

Contents lists available at ScienceDirect

Journal of the Mechanics and Physics of Solids



journal homepage: www.elsevier.com/locate/jmps



Plastic anisotropy and twin distributions near the fatigue crack tip of textured Mg alloys from *in situ* synchrotron X-ray diffraction measurements and multiscale mechanics modeling

Di Xie ^a, Wei Zhang ^a, Zongyang Lyu ^a, Peter K. Liaw ^a, Huy Tran ^b, Huck Beng Chew ^b, Yujie Wei ^c, Yang Ren ^d, Yanfei Gao ^a, *

- ^a Department of Materials Science and Engineering, University of Tennessee, Knoxville, TN 37996, USA
- ^b Department of Aerospace Engineering, University of Illinois at Urbana-Champaign, Urbana, IL 61801, USA
- ^c LNM, Institute of Mechanics, Chinese Academy of Sciences, Beijing 100190, China
- ^d Department of Physics, City University of Hong Kong, Kwoloon, Hong Kong, China

ARTICLE INFO

Keywords: In situ synchrotron X-ray diffraction (S-XRD) Mg alloy Fatigue crack Cohesive interface model Crystal plasticity finite element method

ABSTRACT

In spite of many potential applications due to their superior mechanical properties, magnesium alloys still find many practical restrictions primarily due to our limited knowledge of their failure mechanisms. In situ and non-destructive strain measurements on the microstructural scales are critical in understanding the fatigue crack behavior, which has greater advantages than the macroscopic measurements based on replica technique and the small-scale mechanical testing that cannot easily provide a complete view on the synergy of many scale-dependent deformation and failure mechanisms. This work exploits the state-of-the-art synchrotron X-ray diffraction technique to attain in situ strain mapping results, with high spatial resolution, near a fatigue crack tip in the highly textured ZK60 Mg alloy. The accurate measurements in the plastic zone are compared to a micromechanical modeling framework, in which the steady fatigue crack is simulated by an irreversible, hysteretic cohesive interface model and the surrounding plasticity by Hill anisotropic plasticity. The general agreement in the anisotropic deformation fields is reached down to half of the plastic zone size towards the crack tip, while the discrepancy right at the crack tip can be used to develop an inverse model to extract the material-specific fatigue damage evolution in our future work. It is surprisingly noted that twin activities are localized in a narrow band from the tip to the wake of the fatigue crack, irrespective of the crack growth direction of this textured alloy. Such twin-crack interactions are understood here by our crystal plasticity finite element simulations with several representative crystallographic orientations.

1. Introduction

In the past several decades, significant advances have been developed in the studies of structural alloys, which are at the very heart of modern energy and transportation systems, with the help of modern material testing and characterization techniques across many length scales. Simultaneously, the development of new engineering designs and applications brings tremendous new research opportunities and challenges. Of particular importance is the growing interest in understanding the deformation and failure mechanisms

E-mail address: ygao7@utk.edu (Y. Gao).

^{*} Corresponding author.

of Mg alloys due to their rapid utilization in the automotive and aerospace industries. Mg alloys have desirable combined properties of low density, high strength-to-weight ratio, and high specific stiffness. The unique nature of their hexagonal-close-packed (HCP) structure leads to peculiar plasticity properties when compared to commonly used engineering alloys. Most prior studies have focused on deformation behavior in simple loading conditions. Under uniaxial loading conditions, the deformation of most Mg alloys at room temperature is mainly dominated by basal $\langle a \rangle$ slip, prismatic $\langle a \rangle$ slip, and $\{10\overline{1}2\}$ extension twins. However, the slip and twin behaviors under multiaxial loading conditions are quite sensitive to the material texture. The interplay between the texture and complex slip/twin systems has been investigated extensively (Kim et al., 2003; Kleiner and Uggowitzer, 2004; Koike et al., 2008; Yin et al., 2021). For example, Koike et al. (2008) reported that the anomalous formation of extension twinning under tensile loading parallel to TD (transverse direction) or RD (rolling direction) in basal textured Mg alloys to accommodate strain incompatibility between soft grains (which deform by strong basal slip activity) and neighboring hard grains. These studies on slip/twin/texture interactions help understand and develop new ways to activate multiple families of slip or twin systems, so that the restriction of Mises condition (i.e., a minimum of five independent slip systems is needed; otherwise, the material becomes brittle, just like in many Mg alloys) can be avoided and the ductility can be improved (Hono et al., 2010; Zou et al., 2018). For example, a Mg-Li alloy leads to a two-phase microstructure, and the deformation incompatibility caused by the basal $\langle a \rangle$ slip in the Mg-rich phase can be remedied by the multiple slip systems in the Li-rich phase (Zou et al., 2018). Furthermore, the use of advanced diffraction techniques has become a standard protocol to identify the deformation mechanisms in Mg alloys, despite many such studies are limited to simple loading conditions (Agnew et al., 2013; Wu et al., 2015, 2016); Liu et al., 2018; Sofinowski et al., 2019). For example, using in situ neutron diffraction and electron backscatter diffraction (EBSD) techniques, Sofinowski et al. (2019) found that different pre-strains or strain path changes can lead to a variety of complex deformation modes, some of which may be beneficial in activating multivariant secondary twinning and improving the ductility limit.

Interplays among microstructure, texture, and various slip/twin systems have been fairly understood in the above test conditions where deformation fields are nominally uniform, but it is not entirely so for their roles in the fracture and fatigue behavior of Mg alloys. We now discuss fracture and fatigue studies of Mg alloys from these two lines of thought.

First, it has been widely recognized that metallic materials are generally toughened intrinsically by inducing a significant plasticzone size ahead of the crack tip, and the shape and size of the plastic zone play an important role in influencing the fatigue crack extension. It is thus of great technical importance to determine the effect of microstructure, texture, and slip/twin modes on the development of the plastic zone during the fatigue crack growth, which is termed as the "clean" process zone in this work. Earlier reports reveal that the specimen orientation has a significant influence on the fatigue crack growth rate and crack path. Han et al. (2014) reported that more twins are observed in the transverse direction (TD) specimens (loading axis perpendicular to the extruded direction) than in the extruded direction specimens (loading axis parallel to the extruded direction). Prasad et al. (2015) conducted a detailed microstructural characterization of a rolled Mg plate under Mode-I fracture condition, and found a flat fracture surface in the midplane of the plate but slant fractures close to the free surfaces. The deformed texture changed significantly near the free surfaces, which in turn affect the subsequent twinning behavior, i.e., less tensile twinning near the midplane than that close to free surfaces. Kaushik et al. (2014a), (2014b) have performed Mode-I fracture tests on magnesium single crystals using three notched three-point-bend (TPB) specimens with different orientations. Although extension twins were observed in these three samples, the patterns of twin development for the samples are different. Twins initially formed near the specimen edge ahead of the notch root and then extended toward it with the increase of load for the sample with c-axis oriented along the notch direction, while twins spread out from the notch root in the other two samples with basal plane aligning with notch direction. However, most previous studies, are limited to surface-based characterizations of cracks (Zhang et al., 2011a, 2021b), and the lack of non-destructive bulk measurements unavoidably cast limitation on the correlation between micromechanism and fatigue performance. In recent two decades, a number of studies have employed the modern diffraction techniques (neutron and synchrotron X-ray diffractions, to be specific) to obtain an in situ, non-destructive mapping of the entire elastic strain fields near the fatigue crack tip, e.g., the study of overload effects on the fatigue crack growth behavior in commercial stainless steels or aluminum alloys (Zhang et al., 2019; Barabash et al., 2008; Steuwer et al., 2010; Lee et al., 2010a, 2011b) and the lattice strain distribution near the fatigue crack tip of HCP zirconium alloys (Kerr et al., 2010). Here in this work, we will aim to report a full field mapping in a heavily textured Mg alloy with various fatigue crack growth directions, and thus provide an experimental set of information for the deconvolution of texture and deformation-mode effects in our fundamental understanding of the plastic process zone.

Second, the quantitative characterization of damage processes right at the fatigue crack tip, termed as the "messy" process zone in this work here, is extremely challenging and not easily amenable to traditional experimental methods. Based on the synchrotron X-ray tomography, Withers (2015) has summarized the latest progress on the direct observation of the crack growth front and other defects such as voids on the micrometer resolution. Such measurements for the fatigue crack growth behavior of Mg alloys are limited. One successful example can be found in the work of King et al. (2011), which carefully traced the interactions between crack front and grain boundaries, and therefore enriched the previous modeling work by Zhai et al. (2000) on the fatigue crack path selection in Mg alloys. However, these studies cannot determine the crack resistance, or provide insightful strategies in microstructural and texture design for the control of the fatigue crack growth rate. A statistically homogenized view of these damage processes is thus needed to connect to the plasticity-induced resistance to crack growth. In this work, our attempt along this line will be restricted to a phenomenological cohesive zone approach that helps generate a steady fatigue crack. As will be shown later in this paper, the simulated clean process zone due to plastic deformation agrees very well with experimental measurements of the chosen textured Mg alloy, while the differences on the messy process zone could be used as inputs for an inverse analysis (Hong et al., 2009; Chew et al., 2009) to extract a cohesive interface relationship that represents the actual damage processes. The latter will be presented in our subsequent work.

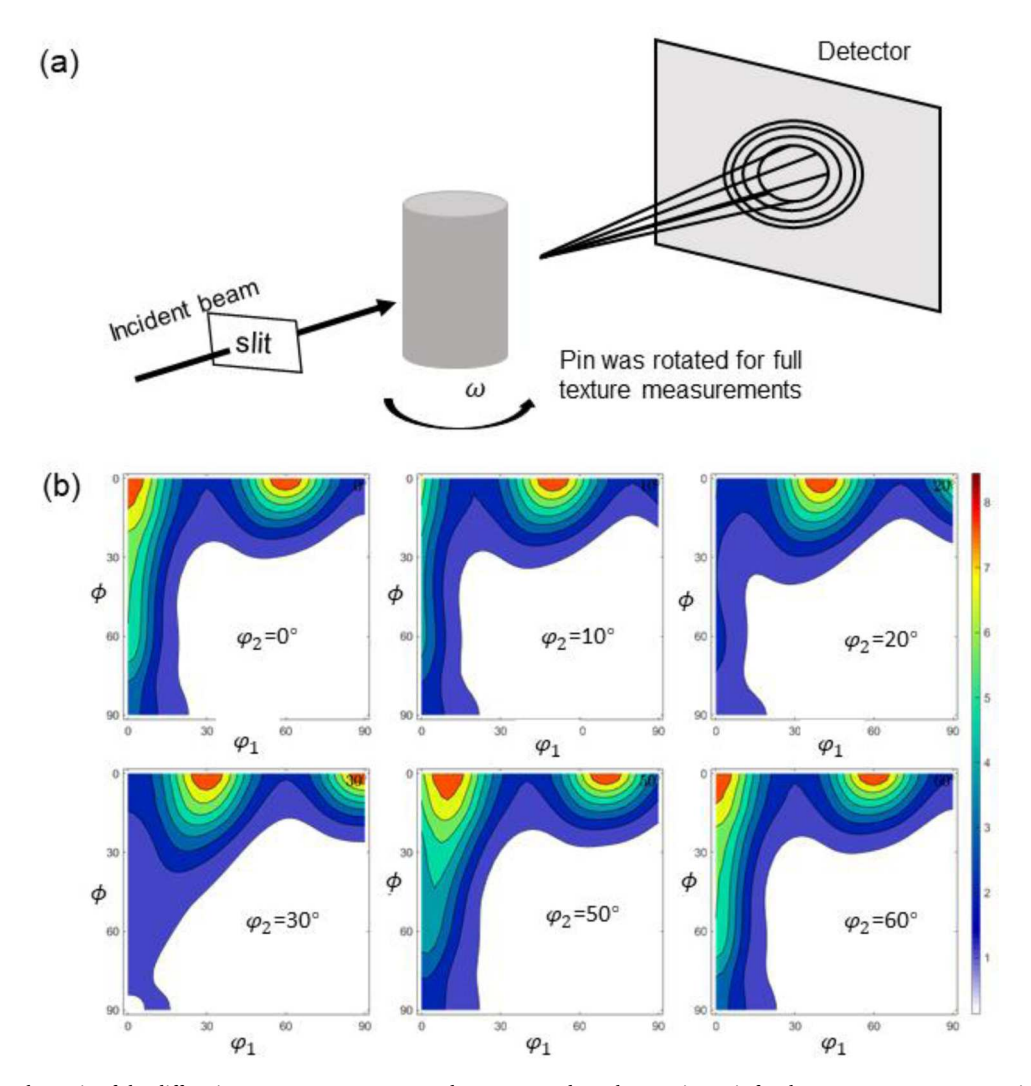


Fig. 1. (a) A schematic of the diffraction measurement set-up and ω corresponds to the rotation axis for the texture measurement using S-XRD, (b) orientation distribution function (ODF) in the $[0, 10^{\circ}, 20^{\circ}, 30^{\circ}, 50^{\circ}]$ sections of φ_2 .

In this paper, synchrotron X-ray diffraction (S-XRD) measurements are employed to investigate the deformation fields around a crack tip in a ZK60 Mg alloy sample with strong texture and plastic anisotropy. The high energy X-ray can easily penetrate through most engineering alloys, the use of 100 µm beam size provides the capability of spatial mapping, and the XRD measurements can be analyzed to decouple the contributions from twinning and dislocation slip to the overall plastic deformation (Kerr et al., 2010; Withers, 2015). All these features, together with the in situ loading and measurements, make is ideal for the use of S-XRD for our problem of interest. During the fatigue crack growth, we note that the stress multiaxiality becomes increasingly more complex along the crack path (Steuwer et al., 2010). Consequently, a material point in the vicinity of a fatigue crack tip will experience a complex history of multiaxial stress states, which has significant implications on the plastic deformation of Mg alloys at the macroscopic scale (i. e., texture design leading to anisotropic plasticity that potentially resists the crack growth much more in some certain directions) and the mesoscale (i.e., deformation of a finite number of grain aggregates around the crack tip to accommodate the multiaxial stress fields). A full-field strain mapping to understand the above complex stress history in the plastic zone is essential for the fatigue-crack-growth studies in Mg alloys. The small plastic zone around the crack tip requires a small beam size with a high spatial resolution to resolve the difference between the plastic zone near the crack tip and the surrounding area - this is ideal for S-XRD experiments. Furthermore, a simulated steady fatigue crack will be developed by an irreversible, hysteretic cohesive interface model to study the stress/strain distributions near the crack tip for the anisotropic plastic material used in this study, and the crystal plasticity finite element method (CPFEM) will be used to understand the twin distributions that are found to surprisingly localize in the plastic wake.

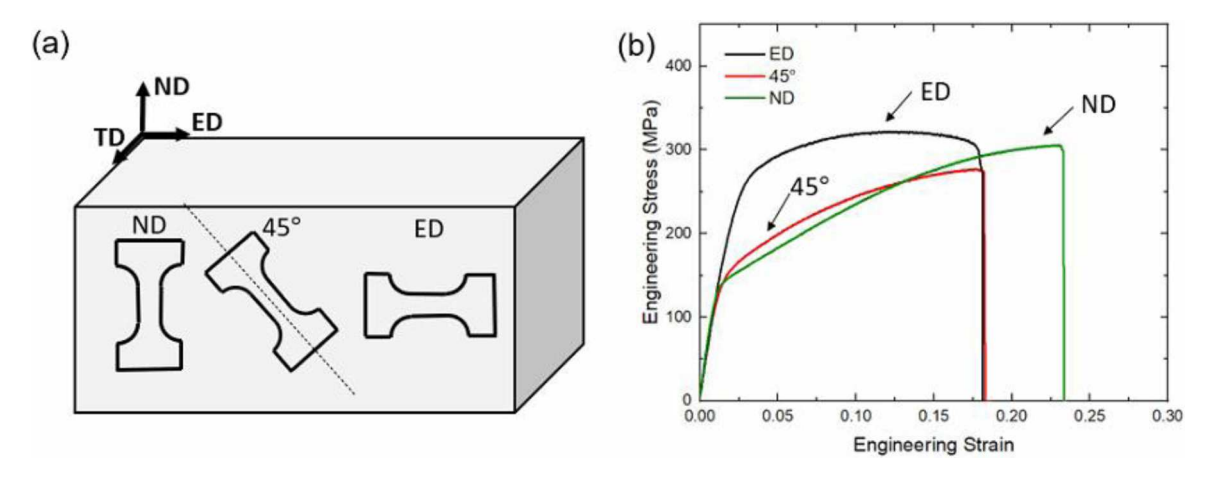


Fig. 2. (a) Three tension samples of extruded ZK60 Mg alloy, oriented differently with respect to the extrusion direction, (b) stress-strain curves for the extruded ZK60 Mg alloy with different loading orientations.

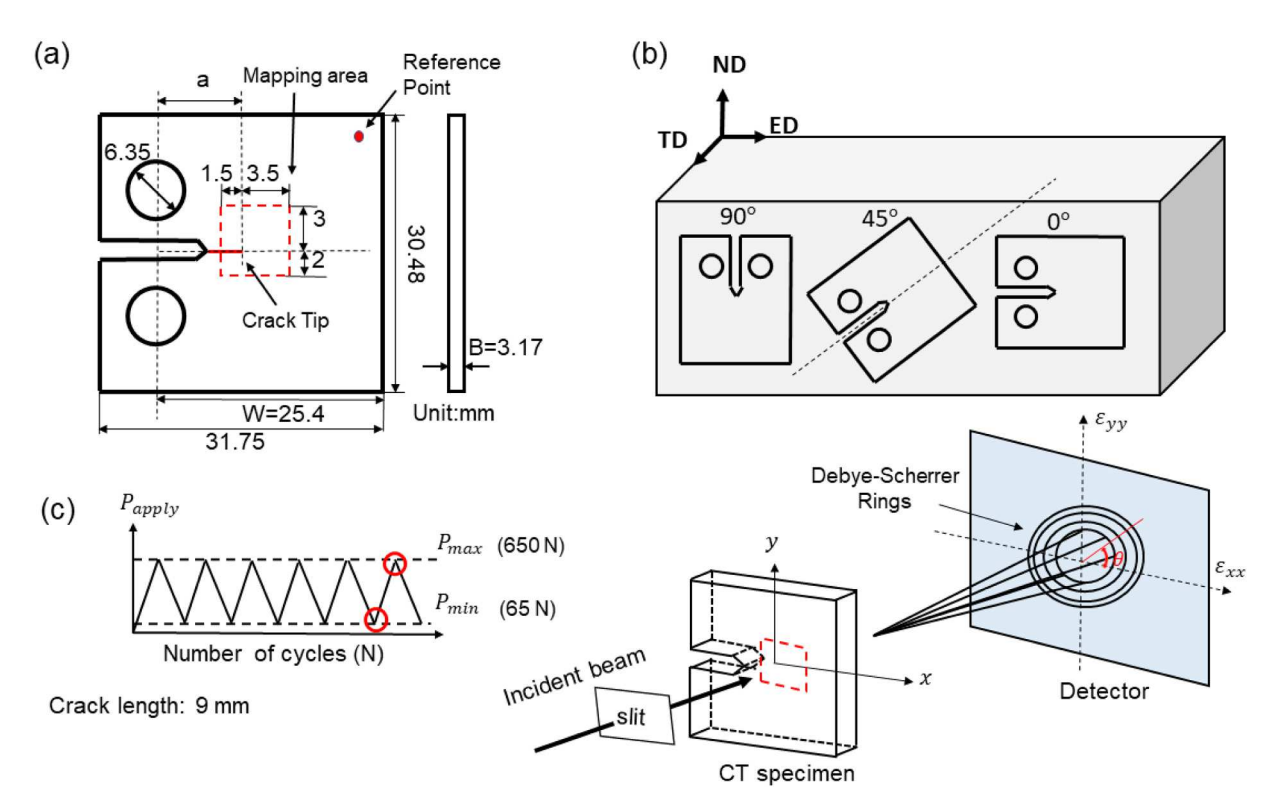


Fig. 3. (a) CT specimen geometry and schematic of the strain mapping area in the red dashed square, (b) three compact tension (CT) specimens of extruded ZK60 Mg alloy, oriented differently with respect to the extrusion direction, and (c) a schematic of the diffraction measurement setup for strain mapping measurement using S-XRD, where *x* presents the crack growth direction, and *y* presents the crack opening direction.

2. Methods

2.1. Materials

The ZK60 Mg alloy with the T5 temper is used in this work. This material is fabricated by an extrusion process with a width of 279.4 mm and a thickness of 76.2 mm. The S-XRD technique was utilized to measure the initial crystallographic texture and lattice strain distributions of ZK60 Mg alloy at the beamline 11-ID-C, the Advanced Photon Source (APS), Argonne National Laboratory (ANL). The wavelength employed during the S-XRD measurement was 0.1173 Å and the sample to detector distance was 1800 mm. The texture

data was collected by mounting the pin sample on a rotary stage and by rotating from 0° to 180° with a 30° step size, obtaining full pole coverage, as schematically shown in Fig. 1(a). The Debye-Scherrer rings were converted into diffraction patterns using the Fit2D software, and then the Material Analysis Using Diffraction (MAUD) software was used to analyze these diffraction data and get the raw pole figure data by performing Rietveld refinement (Lutterotti et al., 1997). MTEX quantitative texture analysis software (Bachmann et al., 2010) was employed to plot the orientation distribution function (ODF) of the ZK60 alloy. By checking the ODF in the [0, 10° , 20° , 30° , 50° , and 60°] sections of φ_2 in Fig. 1(b), this alloy exhibits a combination of strong $\{0001\}<10\overline{1}0>$ rolling texture and weak $<10\overline{1}0>$ fiber. The grain size of this Mg alloy is about 7 ± 4 µm. Uniaxial dog-bone tensile samples were cut on the extruded direction (ED)-normal direction (ND) plane with the longitudinal direction parallel to ED, ND, and 45° between the ED and ND in Fig. 2(a). The uniaxial stress-strain curves are shown in Fig. 2(b), which yield a 0.2% offset strength ~ 260 MPa parallel to the ED, ~ 145 MPa parallel to the ND, and ~ 153 MPa parallel to the $\sim 45^{\circ}$ direction between the ED and ND.

2.2. Fatigue-crack-growth test

To analyze the effect of texture on the fatigue crack propagation behavior of Mg alloys, a series of compact-tension (CT) specimens, prepared according to the American Society of Testing and Materials (ASTM) Standards E647-99 (31) with the geometry shown in Fig. 3(a), were cut on the ED-ND plane with the notch direction parallel to ED, ND, and the 45° between the ED and ND, as shown in Fig. 3(b). They are thus denoted as 0° sample, 45° sample, and 90° sample, respectively. Actual fatigue-crack growth tests were performed under cyclic loading at f=10 Hz at a constant load ratio R=0.1 at room temperature using a Materials Testing System (MTS) 810 servo-hydraulic machine. The CT specimens were pre-cracked to a crack length of 7 mm with a K (stress-intensity factor, $K_{max}=10$ MPa \sqrt{m} , $K_{min}=1$ MPa \sqrt{m}) control mode and then further crack to 9 mm under a constant-load ΔP control mode [$\Delta P=P_{max}-P_{min}$, where P_{max} and P_{min} are the applied maximum (650 N) and minimum (65 N) loads, respectively]. The crack length was measured by a crack-opening-displacement (COD) gauge (ASTM E 647-99, 2016), and then further confirmed by scanning electron microscopy (SEM). The stress-intensity factor (K) can be obtained by the following equation (ASTM E 647-99, 2016):

$$K = \frac{P(2+\alpha)}{B\sqrt{W}(1-\alpha)^{1.5}} \left(0.886 + 4.64\alpha - 13.32\alpha^2 + 14.72\alpha^3 - 5.6\alpha^4\right)$$
 (1)

where P is applied load, B is the thickness, W is the width, and α is the ratio of crack length and width. The cracked CT samples were then taken for the *in situ* S-XRD strain mapping.

2.3. In situ S-XRD measurement

In situ S-XRD measurement of the strain field around the crack tip with a crack length of 9 mm was performed at two load levels, P_{min} (65 N) and P_{max} (650 N). The setup of the strain mapping is schematically shown in Fig. 3(c), and the strain mapping area is pointed out by the red dashed square in Fig. 3(a), which, horizontally, covers from -1.5 mm to +3.5 mm, and, vertically, from -2 mm to +3 mm by setting the crack tip to be the reference point (0, 0). To accurately evaluate the strain, the beam size of 100 μ m \times 100 μ m with a step of 100 μ m was used in this measurement. For each load level, we held the sample and conducted the strain mapping. The holding time during the S-XRD data acquisition period did not affect the deformation behavior since creep was negligible at room temperature. The General Structure Analysis System (GSAS) II software (Toby and Von Dreele, 2013) was used to reduce the diffraction rings and obtain the diffraction patterns by azimuthally averaging the ring pattern over \pm 5° with respect to a series of θ values ($\theta = 0$ °, 45°, and 90°). θ is the angle as defined in Fig. 3(c). The lattice strains were calculated according to the following equation:

$$\varepsilon_{hkl} = \frac{d_{hkl} - d_{hkl}^0}{d_{hkl}^0} \tag{2}$$

where d and d_{hkl}^0 are the strained and unstrained d_{hkl} spacings for a specific grain group, respectively. The d spacings were determined by the Rietveld-fitting for these three samples in this work. The unstrained d_0 was measured at the edge of each CT sample, marked with a red dot in Fig. 3(a), where we assume no deformation occurred. According to Wu et al. (2015), the strain tensor (ε_{ij}) can be determined by fitting the angular variation of ε_i to the following expression:

$$\varepsilon_i = \varepsilon_{xx} cos^2(\theta_i) + 2\varepsilon_{xy} cos(\theta_i) sin(\theta_i) + \varepsilon_{yy} sin^2(\theta_i)$$
(3)

where ϵ_{xx} , ϵ_{yy} and ϵ_{xy} represent the strain along the crack growth direction, crack opening direction, and shear strain, respectively.

2.4. Finite element simulations

A cohesive interface model is used to develop a steady fatigue crack to investigate the stress/strain distributions near the crack tip for ZK60 Mg alloy with strong plastic anisotropy. A typical interface constitutive law relates the tractions acting on two-bonded interfaces to the separation between them. In order to realize a steady fatigue crack numerically, an irreversible, hysteretic cohesive interface model is introduced based on Nguyen et al. (2001) and further modified in Zheng et al. (2011), Gao (2016), which can phenomenologically accumulate crack tip damage and dissipate fracture energy during the fatigue cycles. The relationship between the normal traction T_n and the normal separation Δ_n is given by the following equation:

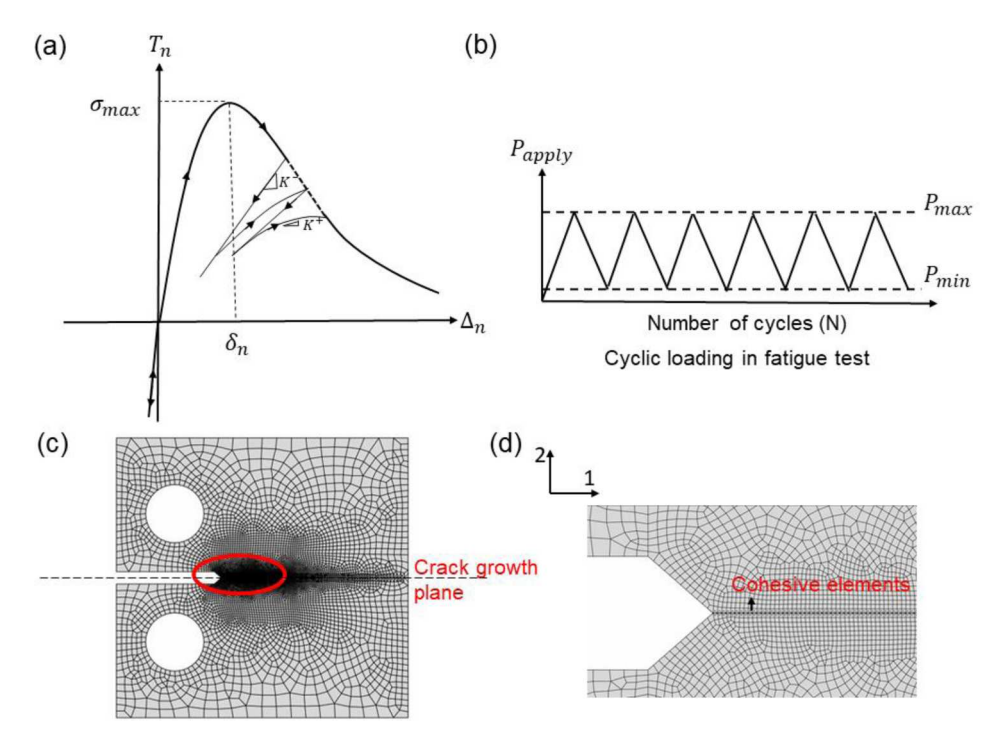


Fig. 4. (a) Traction-separation $(T_n - \Delta_n)$ relationship in the irreversible, hysteretic cohesive interface model, where the unloading process corresponds to a straight line extending through the coordinate origin, and the loading process exhibits a gradual softening behavior, (b) The applied cyclic loading levels with a ratio of $P_{min}/P_{max} = 0.1$, which result in the alternating stress intensity factors, K_{min} and K_{max} , (c) Cohesive interface simulations of a CT specimen (The geometric sizes are taken from Fig. 3), and (d) Enlarged view of the cohesive element on the crack tip.

$$\frac{T_{n}}{\sigma_{\max}} = \frac{\Delta_{n}}{\delta_{n}} \exp\left(1 - \frac{\Delta_{n}}{\delta_{n}}\right) \tag{4}$$

where T_n and Δ_n represent the interface traction and interface separation, respectively, σ_{max} is the interface strength, and δ_n is a characteristic length scale. Then the unloading-reloading hysteresis is introduced by considering the unloading stiffness, K^- , and the reloading stiffness, K^+ , separately,

$$\dot{T}_{n} = \left\{ \begin{array}{ll} \mathbf{K}^{-}\dot{\Delta}_{n}, \ \dot{\Delta}_{n} & < 0 \\ \mathbf{K}^{+}\dot{\Delta}_{n}, \ \dot{\Delta}_{n} & > 0 \end{array} \right. \tag{5}$$

$$K^{-} = \frac{T_{n}^{\text{unload}}}{\Delta_{n}^{\text{unload}}}$$
 (6)

$$\dot{\mathbf{K}}^{+} = \left\{ \begin{array}{l} (\mathbf{K}^{+} - \mathbf{K}^{-})\dot{\Delta}_{n}/\delta_{a}, \ \dot{\Delta}_{n} < 0 \\ -\mathbf{K}^{+}\dot{\Delta}_{n}/\delta_{f}, \ \dot{\Delta}_{n} > 0 \end{array} \right.$$
 (7)

where δ_a and δ_f are length parameters that are associated with the damage behavior during the unloading and reloading process, and T_n^{unload} and Δ_n^{unload} are the normal traction and separation at the unloading point, resulting in a constant K^- at each unloading point. The above relationship is schematically shown in Fig. 4(a). The interface model in Eqs. (4)–(7) has been implemented as a user-defined element (UEL) subroutine in the commercial finite element (FE) software, ABAQUS Documentation (2017). One hidden issue in cohesive zone simulations is the snap-back instability when the calculated crack bridging size is significantly smaller than the crack size. The resulting numerical divergence problem can be avoided by introducing a fictitious viscosity to the above Eq. (4); details on this procedure can be found in Gao and Bower (2004).

In the finite element simulation setup, a standard CT specimen adopted the same geometry in Fig. 3(a) is used to simulate the fatigue crack, which is also subjected to cyclic loading of 65-650 N ($P_{max}/P_{min} = 0.1$), as schematically shown in Fig. 4(b). The representative mesh of the CT sample is shown in Fig. 4(c) and (d), where the cohesive interface element is introduced along the crack growth plane while the surrounding medium is elasto-plastic. The element size should be smaller than the crack bridging size (roughly scaled as $E\sigma_{max}/\delta_n$).

The material plasticity can be modeled by a continuum version without consideration of microstructure and texture. The strong plastic anisotropy in extruded Mg alloys (e.g., Fig. 2) can be faithfully modeled by the Hill plasticity, as will be given in details in Section 3.5.1. The inputs to the Hill plasticity will be the stress-strain curves with respect to various loading directions, while other

Table 1Slip and twin systems in the HCP crystal plasticity finite element model.

Deformation system	System
Basal <a> slip	$\{0001\}\langle 11\overline{2}0\rangle$
Prismatic <a> slip	$\{1\overline{1}00\}\langle11\overline{2}0\rangle$
Pyramidal <a> slip	$\{1\overline{1}01\}\langle11\overline{2}0\rangle$
Pyramidal $\langle a+c \rangle$ slip	$\{11\overline{2}2\}\langle\overline{11}23\rangle$
Extension Twinning	$\{10\overline{1}2\}\langle\overline{1}011\rangle$
Compression Twinning	$\{\overline{1}011\}\langle\overline{1}012\rangle$

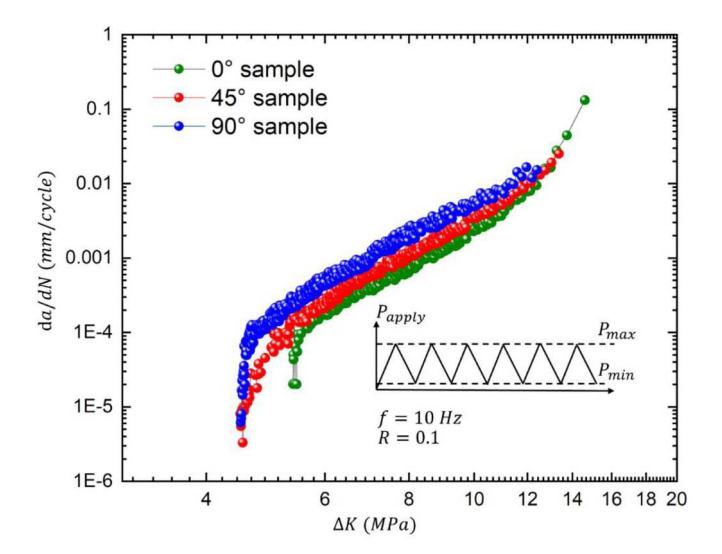


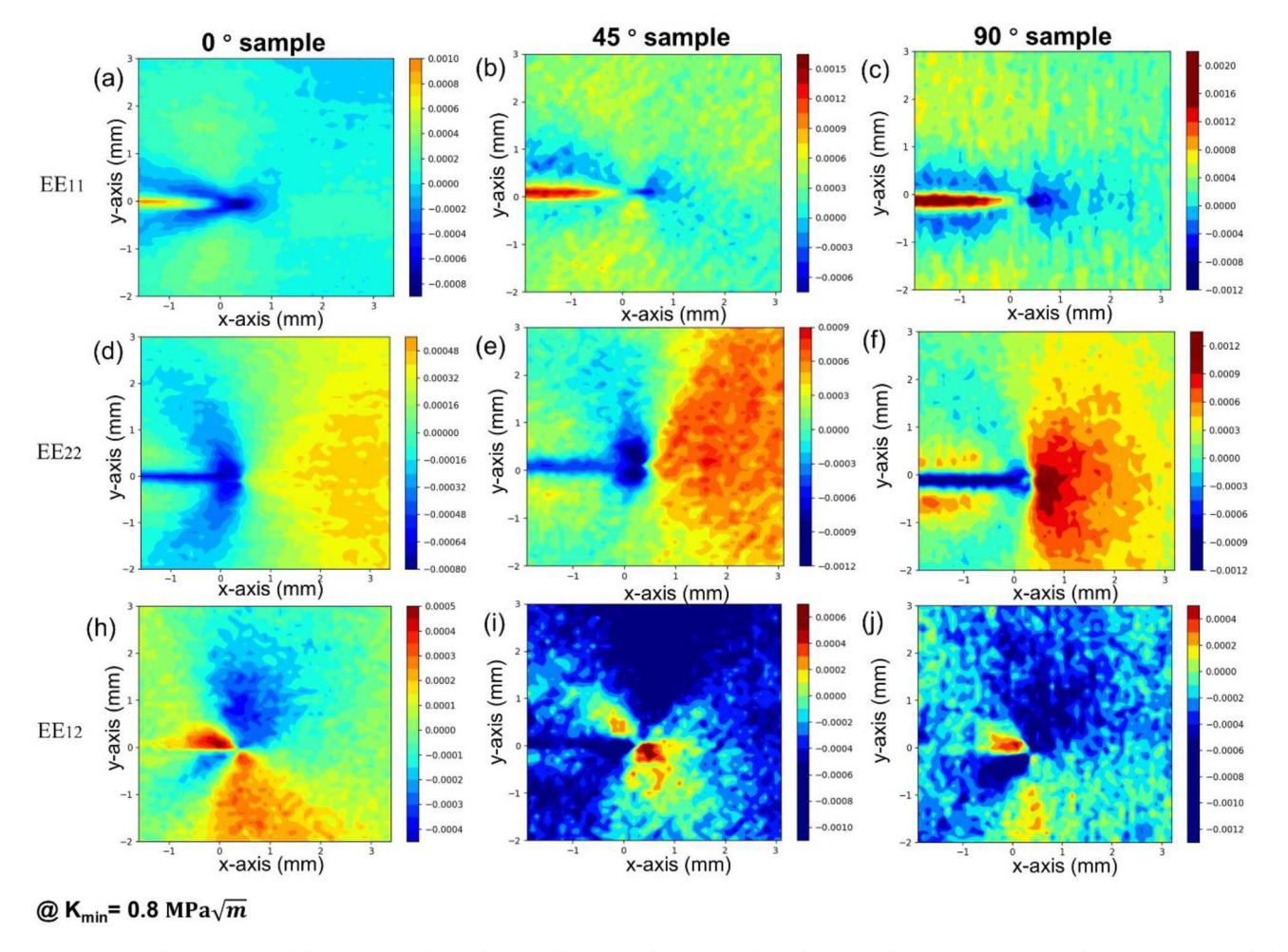
Fig. 5. Fatigue crack growth rate (da/dN) with applied stress intensity factor (ΔK) for the 0° sample, 45° sample, and 90° sample.

secondary factors such as Bauschinger effect or cyclic plasticity are neglected. Combining the classic Hill plasticity and the above ad hoc cohesive interface model is sufficient to reproduce the "clean" process zone. On the other hand, a microstructure-scale simulation requires a polycrystalline setup and a crystal plasticity finite element method (CPFEM) that accounts for both slip and twinning behavior. It is not computationally tractable to simulate the fatigue crack growth by combining CPFEM and our cohesive interface model, merely due to the astronomical mesh number when spatially resolving the grain scale. However, towards the end of this paper, we present a simplified CPFEM simulation on a single crystal sample (mimicking the textured polycrystal but to reduce the degrees of freedom), so as to address the twinning distribution around the crack tip of these CT samples (no fatigue crack tip is modeled or cohesive interface method is used here). The detailed procedure of the adopted crystal plasticity theory and its constitutive equations can be found in the work of Staroselsky and Anand (2003), while a brief overview is given in the Appendix. The total slip and twinning systems considered in the constitutive model are listed in Table 1. The constitutive equations are implemented into the finite element software ABAQUS explicit through a user-defined material subroutine (VUMAT).

3. Results

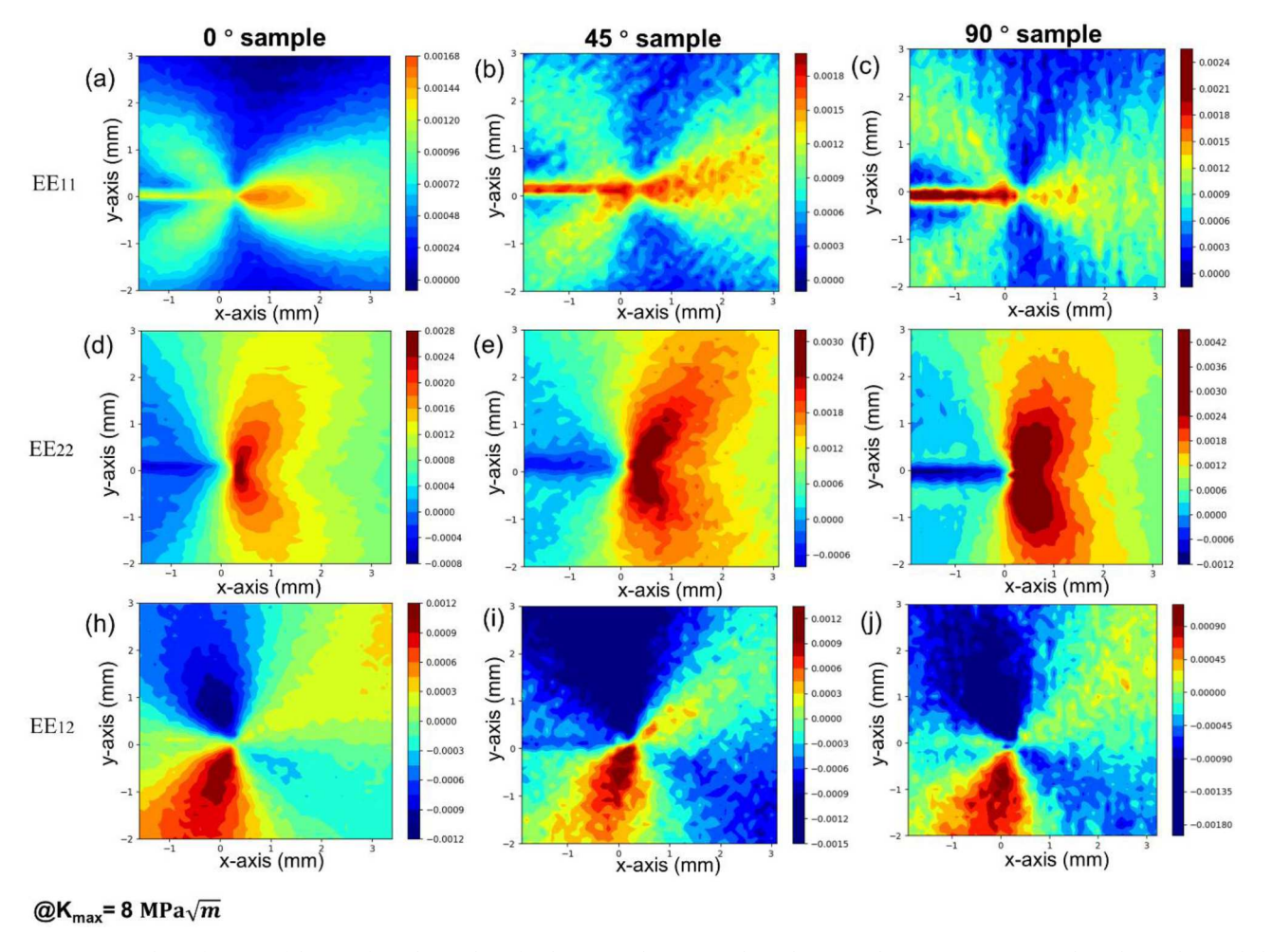
3.1. Fatigue-crack propagation behaviors

Fig. 5 presents the fatigue-crack-growth rate (da/dN) as a function of ΔK for the 0° sample, 45° sample, and 90° sample. The fatigue crack growth characteristics of the three samples are broadly similar to each other in that the crack-growth rate increased linearly with increasing ΔK in the steady fatigue crack growth region, which follows the Paris law. However, when the steady fatigue crack propagation is achieved, the 90° sample presents the largest crack-growth rate, and the 0° sample exhibits the smallest crack-growth rate. The values of the threshold stress intensity factor are approximately the same for the 45° sample and the 90° sample, while a relatively large value is observed for the 0° sample. Hence, specimen orientation has a significant influence on crack growth, especially in the threshold value. Such orientation dependence in the fatigue-crack-growth rate has been reported in Mg alloys (Han et al., 2014). However, further investigation on reasonable factors affecting its fracture resistance has not yet been extensively examined.



œ

Fig. 6. Lattice strain contours measured as a function of distance from the crack tip for the 0° sample, 45° sample, and 90° sample at K_{min} : (a–c) strain along the crack growth direction (EE₁₁); (d–f) strain along the crack opening direction (EE₂₂); (h–j) shear strain around the crack tip (EE₁₂). The (0, 0) coordinate indicates the approximate position of the crack tip.



9

Fig. 7. Lattice strain contours measured as a function of distance from the crack tip for the 0° sample, 45° sample, and 90° sample at K_{max} : (a–c) strain along the crack growth direction (EE₁₁); (d–f) strain along the crack opening direction (EE₂₂); (h–j) shear strain around the crack tip (EE₁₂). The (0, 0) coordinate indicates the approximate position of the crack tip.

3.2. Lattice strain and stress fields and their evolution near a fatigue crack tip

The spatially resolved lattice strain mapping results along the crack growth direction (EE₁₁), crack opening direction (EE₂₂), and shear strain (EE₁₂) as a function of the distance from the crack tip for the 0° sample, 45° sample, and 90° sample with a crack length of ~ 9 mm at K_{min} and K_{max} are shown in Fig. 6 and Fig. 7, respectively. It is important to note that the lattice strains measured by diffraction techniques directly are elastic strains on a certain set of grains that satisfy the diffraction conditions, and the lattice strain values here represent the average values over the gauge volume of $100 \times 100 \times 3170 \,\mu\text{m}^3$. The plastic zone size (R_p) can be estimated by the following equation:

$$R_p = \frac{1}{2\pi} \left(\frac{K_I}{\sigma_V} \right)^2 \tag{8}$$

where σ_Y is the yield stress (~ 260 MPa along with ED, ~ 145 MPa along with ND, and ~ 153 MPa along 45° between the ED and ND), and K is the stress intensity factor, calculated according to Eq. (1), which yields a value of ~ 8 MPa \sqrt{m} at P_{max} and ~ 0.8 MPa \sqrt{m} at P_{min} for these three samples with a crack length of 9 mm. Therefore, according to Eq. (8), the 90° sample has a relatively small plastic zone at K_{max} , compared with that in the 0° sample, and the 45° sample. Given the 100 μ m×100 μ m beam size and 100 μ m step size in the diffraction mapping, the diffraction measurement can capture the millimeter-sized plastic zone ahead of the crack tip at K_{max} .

The lattice strains in these three samples are examined with particular emphasis on the similarities and differences between the contours of lattice strain caused by the plastic anisotropy in Mg alloy. The general characteristics in the lattice strain field evolution are similar in these three samples. Compressive residual strain fields at the crack tip are observed in both the EE_{11} contour and EE_{22} contour in these three samples at K_{min} in Fig. 6. The compressive lattice strain, EE_{22} , along the crack path transitions into a tensile zone ahead of the crack tip at K_{min} , for example, ~ 0.3 mm in front of the crack tip in the 0° sample. While the tensile lattice strain, EE_{11} , along the crack path transitions into a compressive zone behind the crack tip at K_{min} . As one might expect, with the increase of load level from P_{min} (or K_{min}) to P_{max} (or K_{max}), the magnitude of lattice strains (EE_{11} , EE_{22} , and EE_{12}), especially ahead of the crack tip, is significantly increased due to the higher stress concentration, as shown in Fig. 7. A tensile lattice strain field, EE_{22} , is developed ahead of the crack tip, while a compressive lattice strain field is still observed behind the crack tip at K_{max} , and the position of the peak strain, EE_{22} , is observed ahead of the crack tip.

Although the general trends of the lattice strain fields are similar in these three samples, there are some differences. Firstly, for the tensile strain fields in both the contours of EE_{11} and EE_{22} at P_{min} in Fig. 6, the largest tensile strain magnitude is observed in the 90° sample, the moderate one in the 45° sample, and the least one in the 0° sample. Secondly, given the same applied P_{max} in Fig. 7, the 90° sample loaded along ED exhibits the largest lattice strain field, EE_{22} , ahead of the crack tip, compared to the 0° sample loaded along with ND and the 45° sample loaded along 45° direction between the ED and ND. This can be explained by the largest 0.2% offset strength parallel to ED, resulting in the greatest elastic strain field in the 90° sample. Thirdly, distinct to the symmetric lattice strain fields (EE_{11} and EE_{22}) on the crack growth plane in the 0° sample and the 90° sample, the asymmetric strain contour is observed in the 45° sample, as displayed in Figs. 6, 7. Both the strain component fields, EE_{11} and EE_{22} , around the crack tip are asymmetric on the crack growth plane in the 45° sample at E_{max} and E_{max}

According to the ASTM E399-90 for linear-elastic plane-strain fracture toughness (40), a crack in a fracture mechanics specimen is likely to undergo plane strain conditions if its thickness (B=3.17 mm) is greater than 2.5 $(K/\sigma_y)^2$, which gives B > 7.6 mm for the 0° sample, B > 6.8 mm for the 45° sample, and B > 2.3 mm for the 90° sample at P_{max} . These thicknesses will be a little bit smaller for the fatigue sample considering the effective stress intensity (K_{Ie}). At first glance, the 0° sample and the 45° sample are under a plane-stress condition, while the 90° sample is in a plane-strain condition at P_{max} ; however, all these samples at P_{max} are in the plane-stress condition, which will be verified by the cohesive interface model in Section 3.5.1. This is due to the plastic deformation near the crack tip, where the linear elastic fracture mechanics (LEFM) does not work anymore in that region. The stress field at P_{min} is calculated using a plane-strain approximation for these samples. As the elastic mechanical response of Mg alloys is nearly isotropic (Wu et al., 2008; Catoor et al., 2013), the relationship between the stress and strain can be expressed as the generalized Hooke's Law:

$$\sigma_{i} = \frac{E}{1+v} \left[\varepsilon_{i} + \frac{v}{(1-2v)} \left(\varepsilon_{x} + \varepsilon_{y} + \varepsilon_{z} \right) \right] \tag{9}$$

where E (= 50 GPa) is the young's modulus, and v (= 0.3) is Poisson's ratio. For the plane-stress state where the $\sigma_{zz} = \sigma_{xz} = \sigma_{yz} = 0$, Eq. (9) can be re-written as a matrix equation:

$$\begin{cases}
\sigma_{xx} \\
\sigma_{yy} \\
\sigma_{xy}
\end{cases} = \frac{E}{1 - v^2} \begin{bmatrix} 1 & v & 0 \\ v & 1 & 0 \\ 0 & 0 & 1 - v \end{bmatrix} \begin{cases} \varepsilon_{xx} \\ \varepsilon_{yy} \\ \varepsilon_{xy} \end{cases} \tag{10}$$

For the plane-strain state where the $\varepsilon_{zz}=\varepsilon_{yz}=\varepsilon_{yz}=0$, Eq. (9) can be re-written as a matrix equation:

$$\begin{cases}
\sigma_{xx} \\ \sigma_{yy} \\ \sigma_{xy}
\end{cases} = \frac{E}{(1+v)(1-2v)} \begin{bmatrix} 1-v & v & 0 \\ v & 1-v & 0 \\ 0 & 0 & 1-2v \end{bmatrix} \begin{cases} \varepsilon_{xx} \\ \varepsilon_{yy} \\ \varepsilon_{xy} \end{cases}$$
(11)

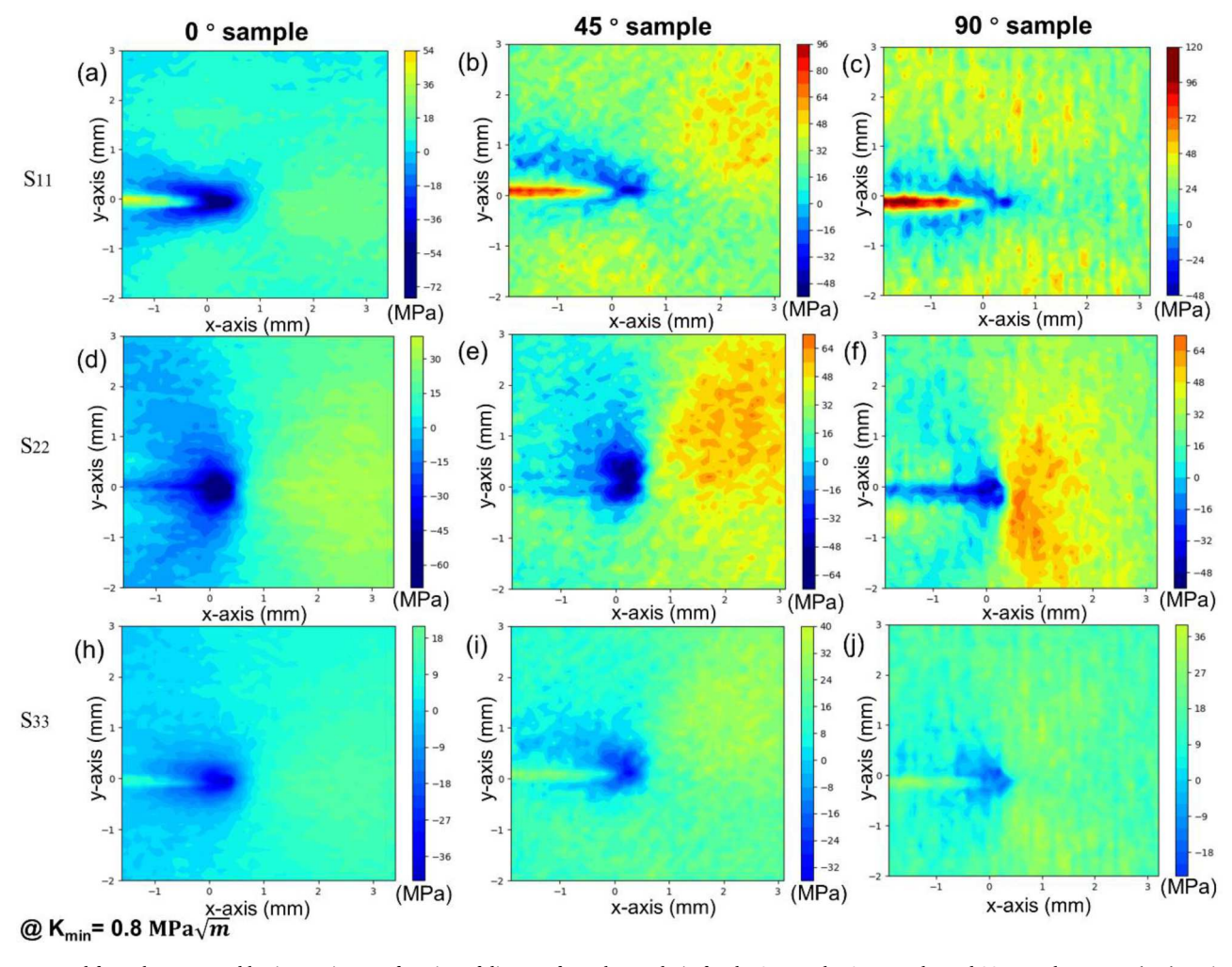


Fig. 8. Stress contours converted from the measured lattice strains as a function of distance from the crack tip for the 0° sample, 45° sample, and 90° sample at K_{min} : (a–c) strain along the crack growth direction (S_{11}); (d–f) strain along the crack opening direction (S_{22}); (h–j) normal to the plate direction (S_{33}). The (0, 0) coordinate indicates the approximate position of the crack tip.

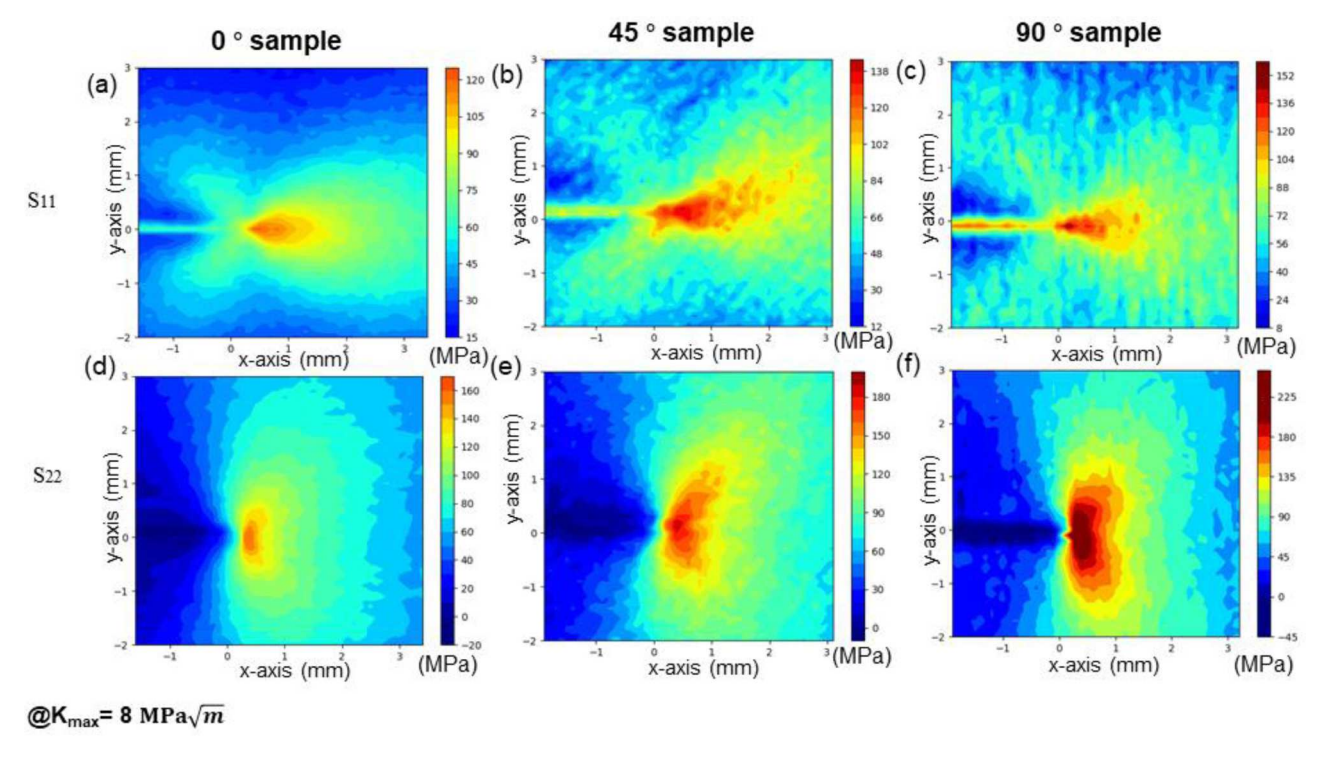


Fig. 9. Stress contours converted from the measured lattice strains as a function of distance from the crack tip for the 0° sample, 45° sample, and 90° sample at K_{max} : (a - c) strain along the crack growth direction (S_{11}) ; (d–f) strain along the crack opening direction (S_{22}) . The (0, 0) coordinate indicates the approximate position of the crack tip.

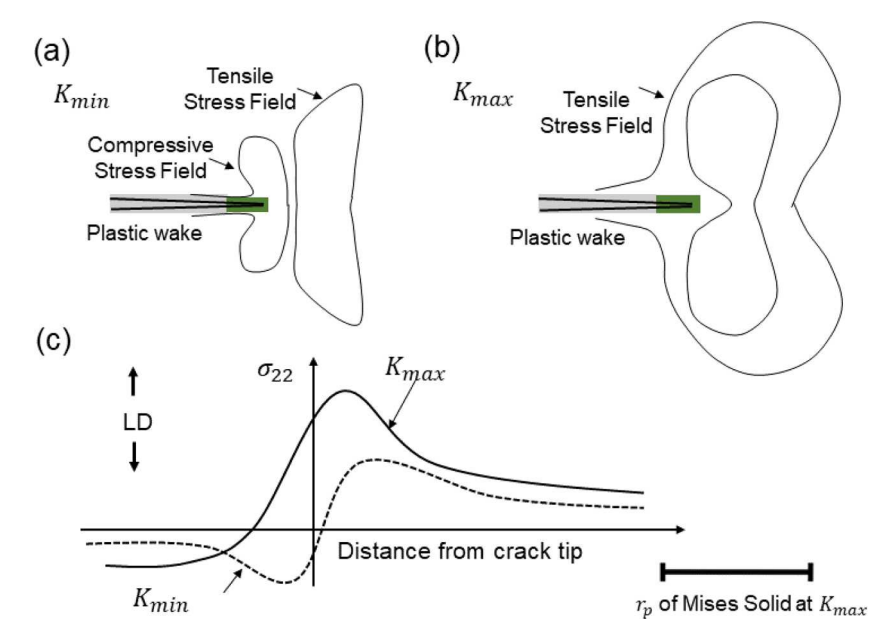


Fig. 10. Schematic illustration of the contours of stress σ_{22} near a steady fatigue crack tip using a Mises plastic model at K_{max} and K_{min} , respectively. (c) Stress σ_{22} evolution along the crack path at K_{min} and K_{max} .

$$\sigma_{zz} = \frac{Ev}{(1+v)(1-2v)} \left(\varepsilon_{xx} + \varepsilon_{yy} \right) \tag{12}$$

The calculated stress distributions converted from the measured lattice strain for these three samples are shown at K_{max} and K_{min} in Fig. 8 and Fig. 9, respectively. All three specimens display analogous tendencies of the stress field evolution along the crack path. Reverse plastic zones with a triaxial compressive stress state ($\sigma_{11} \approx \sigma_{22} \approx 2\sigma_{33}$) at the crack tip are developed in these samples at K_{min} , as displayed in Fig. 8. Our results are consistent with those recorded by Lee et al. (2010) using neutron diffraction for 316 steel that a residual reverse plastic zone is observed at the crack tip. The compressive zones at the crack tip are developed as a result of the prior plastic deformation before unloading. It can be evidently seen from Fig. 9 that the stress multiaxiality near the crack tip transitions from a biaxial tension-compression stress state ($\sigma_{11} \approx -2\sigma_{22}$) in the plastic wake region, and to a biaxial tensile stress state ($\sigma_{11} \approx -2\sigma_{22}$) in the plastic zone region, and to a biaxial tensile stress state in the linear elastic region at K_{max} . A schematic illustration of the deformation fields near a steady fatigue crack tip with Mises plasticity is shown in Fig. 10. Clearly, the increase of the applied stress intensity factor to K_{max} leads to a tensile plastic deformation region in front of the fatigue crack tip, and the unloading from K_{max} to K_{min} results in a reverse compressive residual stress zone at the crack tip. The tensile stress ahead of the crack tip acts as the driving force for crack propagation, while the compressive stress behind the crack tip serves as a crack closure effect that resists crack growth. It is the reduced compressive zone in 90° sample that is mostly responsible for its highest fatigue crack growth rate.

There are also some differences in the stress distribution in the three samples due to the strong plastic anisotropy. Comparing these compressive stress fields around the crack tip at K_{min} , relatively large reverse compressive stress is distributed in a relatively broad zone size in the 0° sample, followed by the 45° sample. The large reverse plastic zone with high negative stress magnitude is more important than crack closure in influencing crack growth (Steuwer et al., 2010; Pippan and Hohenwarter, 2017), which may lead to greater crack-growth retardation in the 0° sample. Similar to the asymmetric contour of lattice strain in the 45° sample, the contours of stress components (S_{11} and S_{22}) also exhibit asymmetry on the crack-growth plane. Furthermore, the contour of the S_{22} in the 90° sample presents the largest peak stress ahead of the crack tip compared to the other two samples at K_{max} , which will accelerate the high fatigue crack propagation rate in the 90° sample.

3.3. Diffraction intensity and twin evolution near a fatigue crack tip

Extension twinning as the most important twinning system has been extensively investigated by diffraction techniques in the past decade (Wu et al., 2008; Brown et al., 2005; Gharghouri et al., 1999). The occurrence of extension twinning can be easily captured by the variation of peak intensity in twin-related crystallographic orientation. i.e., the twin-related (0002) and ($10\overline{10}$) orientations in Mg alloys (Wu et al., 2012a, 2016b, 2008c; Xie et al., 2021). If extension twinning occurs, the (0002) peaks would appear at a relative \sim 90° to the initial (0002) orientation angles due to the reorientation angle of extension twinning at 86.3° (Qiao et al., 2016), as schematically illustrated in Fig. 11(d). The diffraction patterns discussed here are obtained by azimuthally averaging the ring pattern over $\pm 5^\circ$ along the initial ED, that is $\theta = 0^\circ$ (x-direction), 90° (y-direction), and 135° on the Debye-Scherrer rings for the 0° sample, the 90° sample, and the 45° sample, respectively, as shown in Fig. 11. Therefore, there should be no obvious (0002) peaks appearing in the

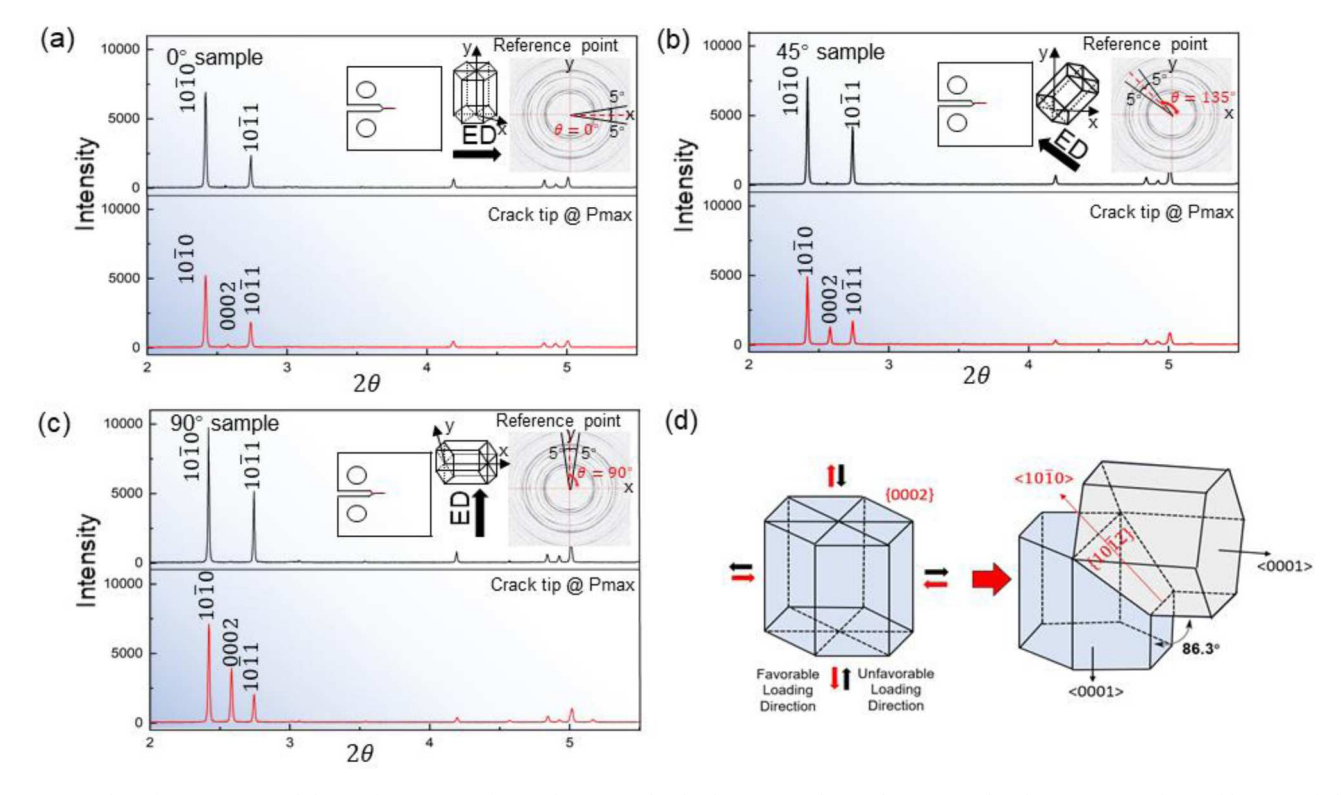


Fig. 11. Diffraction patterns at the reference point and the crack tip at K_{max} for (a) the 0° sample, (b) the 45° sample, (c) the 90° sample. The intensity is obtained by azimuthally averaging the ring pattern over $\pm 5^{\circ}$ with respect to the θ value of 0° , 90° , and 135° on the Debye-Scherrer rings for the 0° sample, the 90° sample, and the 45° sample, respectively, and (d) schematically illustration of grain reorientation due to extension twinning.

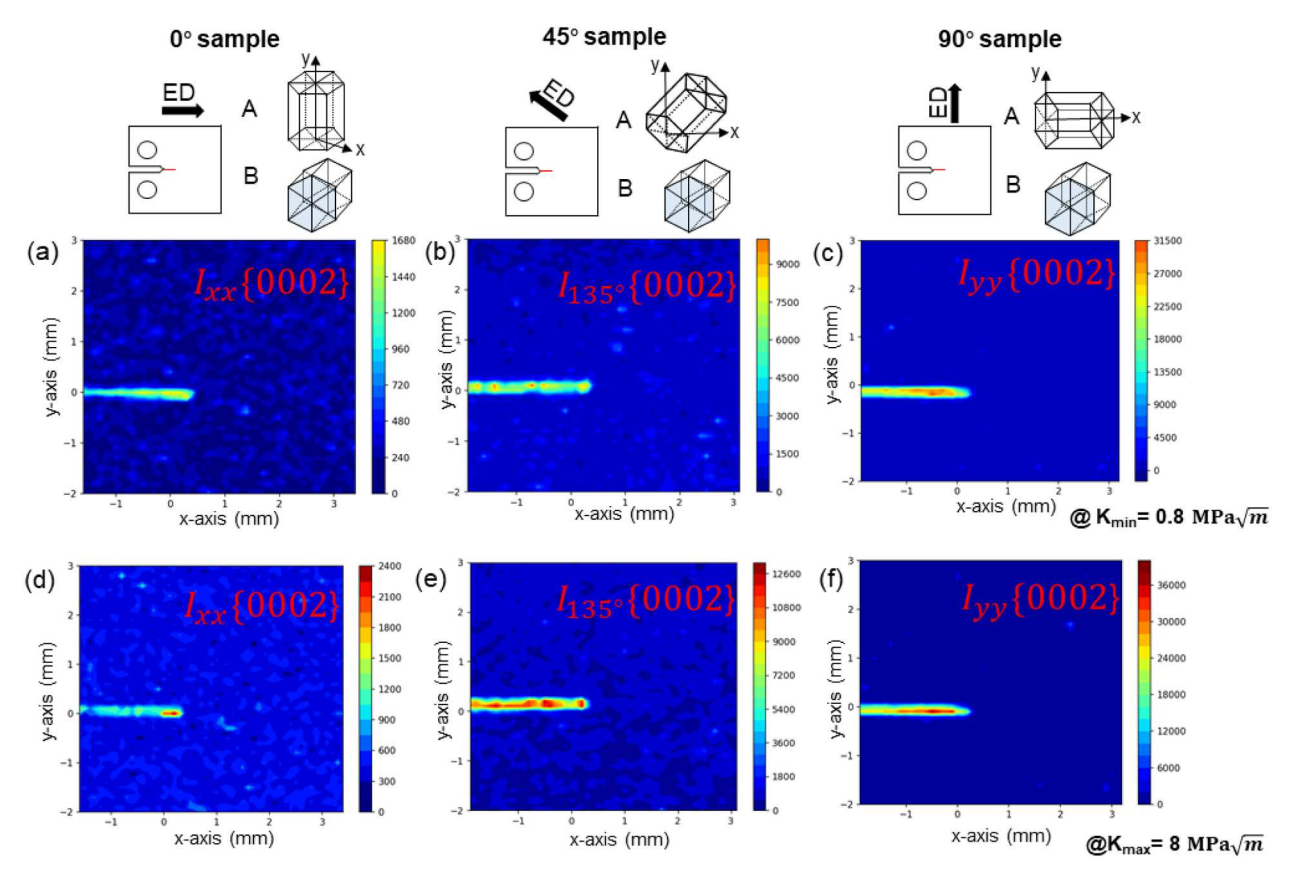


Fig. 12. (0002) intensity evolution with an arbitrary unit at K_{min} and K_{max} for the 0° sample (a) and (d), the 45° sample (b) and (e), and the 90° sample (c) and (f). The (0, 0) coordinate indicates the approximate position of the crack tip. The intensity is obtained by azimuthally averaging the ring pattern over $\pm 5^{\circ}$ with respect to the θ value of 0° , 90° , and 135° on the Debye-Scherrer rings for the 0° sample, the 90° sample, and the 45° sample, respectively.

diffraction pattern before deformation based on the initial texture, and the appearance of (0002) peak on the corresponding diffraction pattern after deformation will be solely related to the extension twinning process. Although there may have other twinning systems that occur during the cyclic loading, i.e., contraction twinning system that usually occurs at very large strain amplitude with small fraction (Zhou et al., 2014), only extension twinning is discussed in this work.

In order to provide a direct picture about the twinning process that is related to the intensity change in the twin-related (0002) and ($10\overline{1}0$) peaks, the diffraction patterns of the reference point (red point in Fig. 3) and crack tip point at P_{max} for these three samples are shown in Fig. 11. No obvious (0002) peaks in the diffraction patterns for the reference points in these three samples are observed as expected. And (0002) peaks appear with the consumption of ($10\overline{1}0$) peak in the diffraction patterns for the crack tip points at P_{max} , which suggests the activation of extension twinning. Taking the initial strong rolling texture component of this alloy into consideration, one may expect to observe extension twinning in the 0° sample (loading along with ND) and 45° sample (loading along 45° between ED and ND) to accommodate the strain along the loading direction (LD), while twinning cannot be activated in the 90° sample (loading along with the ED) due to the far-field tension. This is, however, not the experimental finding. The intensity increment of $\{0002\}$ peak is the largest in the 90° sample, the least in the 0° sample.

Fig. 12 depicts the contours of $I_{xx}\{0002\}$ for the 0° sample, and $I_{yy}\{0002\}$ for the 90° sample, and $I_{135^\circ}\{0002\}$ for the 45° sample at P_{max} and P_{min} . It is interesting to note that I $\{0002\}$ with relatively increased values compared with the weak surroundings only appears in a ~ 200 -300 μm wide band along the crack-growth path at the plastic zone region and behind the crack tip at both K_{max} and K_{min} . This fact suggests the activation of extension twins in the vicinity of fatigue crack surfaces and the formation of a "twin band". Meanwhile, the I $\{0002\}$ on the "twin band", as expected, rises with the increase of applied load from K_{min} to K_{max} (or the decreases with the unloading from K_{max} to K_{min}), suggesting the occurrence of the alternate twinning-detwinning process during the cyclic loading-unloading sequence.

Compared to surrounding materials, the increased magnitude of I{0002} on the "twin band" from the large to small order under a far-field tensile stress state is 90° sample $> 45^{\circ}$ sample $> 0^{\circ}$ sample. This fact suggests that more grains are involved in twinning in the 90° sample, and then the 45° sample, contrary to one's expectation, compared to the 0° sample, which is also confirmed by the optical microscope (OM) image of the deformed samples after S-XRD mapping (Fig. S1 in Appendix). Furthermore, we can notice that the I {0002} behind the crack tip along the "twin band" is weaker than that ahead of the crack tip in the 0° sample and 45° sample, while an opposite trend is observed in the 90° sample. The relatively weak I{0002} behind the crack tip in the 0° sample and 45° sample can result from the accumulation of residual twins formed in the plastic zone region. The greater I{0002} behind the crack tip in the 90° sample, however, cannot solely result from the accumulation of the residual twins at the crack tip. The onset of extension twinning under uniaxial load is generally characterized by critical shear stress (CRSS) (Gharghouri et al., 1999; Wu et al., 2008), whereas the twinning activities under a complex stress state are far more complicated. Based on the initial texture in Fig. 1(b), one may argue that the unexpected intensity variation in these samples can be related to the weak fiber texture, in addition to the strong rolling texture. Two reasons are proposed here to deny this argument. To make our discussion more concisely, two extreme cases for grain orientations are considered here: c-axis parallel to ND (denoted as A-grain, representing the strong rolling texture) and c-axis along with TD (denoted as B-grain, representing one component of the weak fiber texture) in these three samples, as schematically shown in Fig. 12. First, the fraction of the B-grain component is much smaller than of the A-grain component according to the weak extruded texture and strong rolling texture, which means the intensity difference caused by the B-grain component in these samples is negligible. Second, as all three samples have the same weak B-grain component, it is reasonable to speculate that the difference in the fatigue performance and the microstructural evolution in these three samples mainly result from the A-grains. Along this line, the twinning/detwinning behavior in A-grains is the primary contribution promoting the difference of the "twin band". To illustrate the twinning process in the samples with different orientations, a simplified crystal plasticity finite element simulation will be applied to investigate the twin distributions in Section 3.5.2.

3.4. Finite element simulation

3.4.1. Cohesive interface model for fatigue crack growth simulation

To capture the anisotropic mechanical response in the ZK60 alloy, Hill's anisotropic plasticity is adopted for the clean process zone. The quadratic Hill's yield criterion is a simple extension of the Mises function to describe the anisotropic plastic deformation with three orthogonal planes of symmetry, given by a quadratic form (Hill, 1948):

$$f(\sigma) = \sqrt{F(\sigma_{22} - \sigma_{33})^2 + G(\sigma_{33} - \sigma_{11})^2 + H(\sigma_{11} - \sigma_{22})^2 + 2L\sigma_{23}^2 + 2M\sigma_{31}^2 + 2N\sigma_{12}^2}$$
(13)

where σ_{ij} and τ_{ij} represent the normal and shear stress components, respectively; F, G, H, L, M, and N are constants that represent the state of plastic anisotropy.

In ABAQUS, plastic anisotropy is typically represented employing the anisotropic yield stress ratios, $\mathbf{R_{ij}}$ (= σ_{ij}/σ^0) ABAQUS Documentation (2017), which represents the yield stress ratios in the normal (R₁₁, R₂₂, and R₃₃) and shear (R₁₂, R₁₃, and R₂₃) directions. The values of these constants are defined by the following relations:

$$\mathbf{F} = \frac{(\sigma^0)^2}{2} \left(\frac{1}{\overline{\sigma}_{22}^2} + \frac{1}{\overline{\sigma}_{33}^2} - \frac{1}{\overline{\sigma}_{11}^2} \right) = \frac{1}{2} \left(\frac{1}{\mathbf{R}_{22}^2} + \frac{1}{\mathbf{R}_{33}^2} - \frac{1}{\mathbf{R}_{11}^2} \right) \tag{14}$$

Table 2Anisotropic parameters in Hill's yield function in the Abaqus modeling for ZK60 alloy.

R ₁₁	R ₂₂	R ₃₃	R ₁₂	R ₁₃	R ₂₃
1.0	0.558	0.588	0.596	0.596	0.596

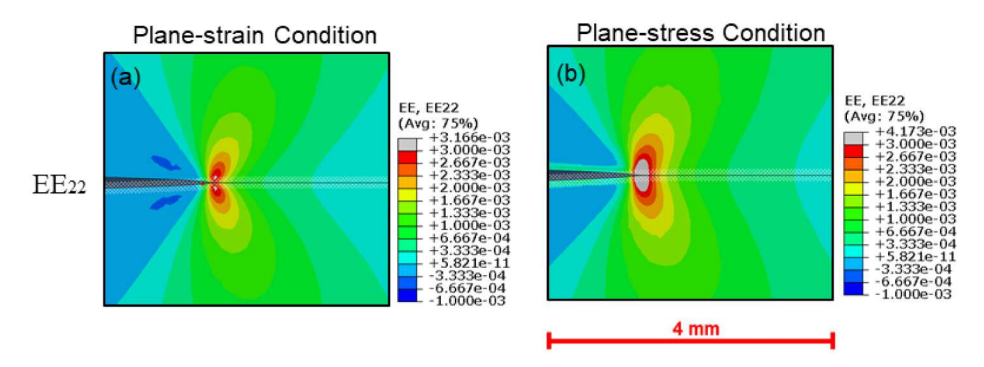


Fig. 13. Contours of elastic strains along the crack opening direction, EE_{22} for 90° sample (a) under the plane-strain condition from FE simulation; (b) under the plane-stress condition from FE simulation. The deformation field is magnified by a factor of 10.

$$\mathbf{G} = \frac{(\sigma^0)^2}{2} \left(\frac{1}{\overline{\sigma}_{32}^2} + \frac{1}{\overline{\sigma}_{11}^2} - \frac{1}{\overline{\sigma}_{22}^2} \right) = \frac{1}{2} \left(\frac{1}{\mathbf{R}_{13}^2} + \frac{1}{\mathbf{R}_{11}^2} - \frac{1}{\mathbf{R}_{22}^2} \right) \tag{15}$$

$$\mathbf{H} = \frac{(\sigma^0)^2}{2} \left(\frac{1}{\overline{\sigma}_{11}^2} + \frac{1}{\overline{\sigma}_{22}^2} - \frac{1}{\overline{\sigma}_{22}^2} \right) = \frac{1}{2} \left(\frac{1}{\mathbf{R}_{11}^2} + \frac{1}{\mathbf{R}_{22}^2} - \frac{1}{\mathbf{R}_{22}^2} \right) \tag{16}$$

$$L = \frac{3}{2} \left(\frac{\tau^0}{\overline{\sigma}_{23}^2} \right)^2 = \frac{3}{2R_{23}^2}$$
 (17)

$$M = \frac{3}{2} \left(\frac{\tau^0}{\overline{\sigma}_{13}^2} \right)^2 = \frac{3}{2R_{13}^2}$$
 (18)

$$N = \frac{3}{2} \left(\frac{\tau^0}{\overline{\sigma}_{12}^2} \right)^2 = \frac{3}{2R_{12}^2}$$
 (19)

where σ^0 is the user-defined reference yield stress and τ^0 is defined as $\sigma^0/\sqrt{3}$. The material properties of the ZK60 alloy in the cohesive interface model are assumed to be elasto-plastic with Young's modulus E=50 GPa, Poisson's ratio $\nu=0.3$, yield strength $\sigma_y=260$ MPa (LD parallel to ED), and strain hardening exponent, N=0.15. And the plastic anisotropy characterized by Hill's potential function in ABAQUS is given in terms of anisotropic yield stress ratios R_{ij} , which can be evaluated by the uniaxial tensile yield strength loading in ED (0°), 45° between ED and ND on the ED-ND plane (45°), ND (90°), and transverse direction (TD), according to the following equations (Wang et al., 2020):

$$\mathbf{F} = \frac{(\sigma^0)^2}{2} \left(\frac{1}{\overline{\sigma}_{200}^2} + \frac{1}{\overline{\sigma}_{210}^2} - \frac{1}{\overline{\sigma}_{20}^2} \right) = \frac{1}{2} \left(\frac{1}{\mathbf{R}_{22}^2} + \frac{1}{\mathbf{R}_{22}^2} - \frac{1}{\mathbf{R}_{11}^2} \right) \tag{20}$$

$$\mathbf{G} = \frac{(\sigma^0)^2}{2} \left(\frac{1}{\overline{\sigma}_{7D}^2} + \frac{1}{\overline{\sigma}_{01}^2} - \frac{1}{\overline{\sigma}_{45}^2} \right) = \frac{1}{2} \left(\frac{1}{\mathbf{R}_{33}^2} + \frac{1}{\mathbf{R}_{11}^2} - \frac{1}{\mathbf{R}_{22}^2} \right) \tag{21}$$

$$\mathbf{H} = \frac{(\sigma^0)^2}{2} \left(\frac{1}{\overline{\sigma}_{01}^2} + \frac{1}{\overline{\sigma}_{20}^2} - \frac{1}{\overline{\sigma}_{1D}^2} \right) = \frac{1}{2} \left(\frac{1}{\mathbf{R}_{11}^2} + \frac{1}{\mathbf{R}_{22}^2} - \frac{1}{\mathbf{R}_{33}^2} \right) \tag{22}$$

$$\mathbf{N} = (\sigma^0)^2 \left(\frac{2}{\overline{\sigma}_{45^\circ}^2} - \frac{1}{2\overline{\sigma}_{1D}^2} \right) = \frac{3}{2\mathbf{R}_{12}^2}$$
 (23)

Through-thickness anisotropic parameters related to shear L and M are assumed to be identical to the anisotropic parameters of N. By assuming the $R_{11} = 1$, the anisotropic parameters R_{ij} in the yield function are listed in Table 2. The mathematic derivation process is elaborated in Ref. Wang et al. (2020).

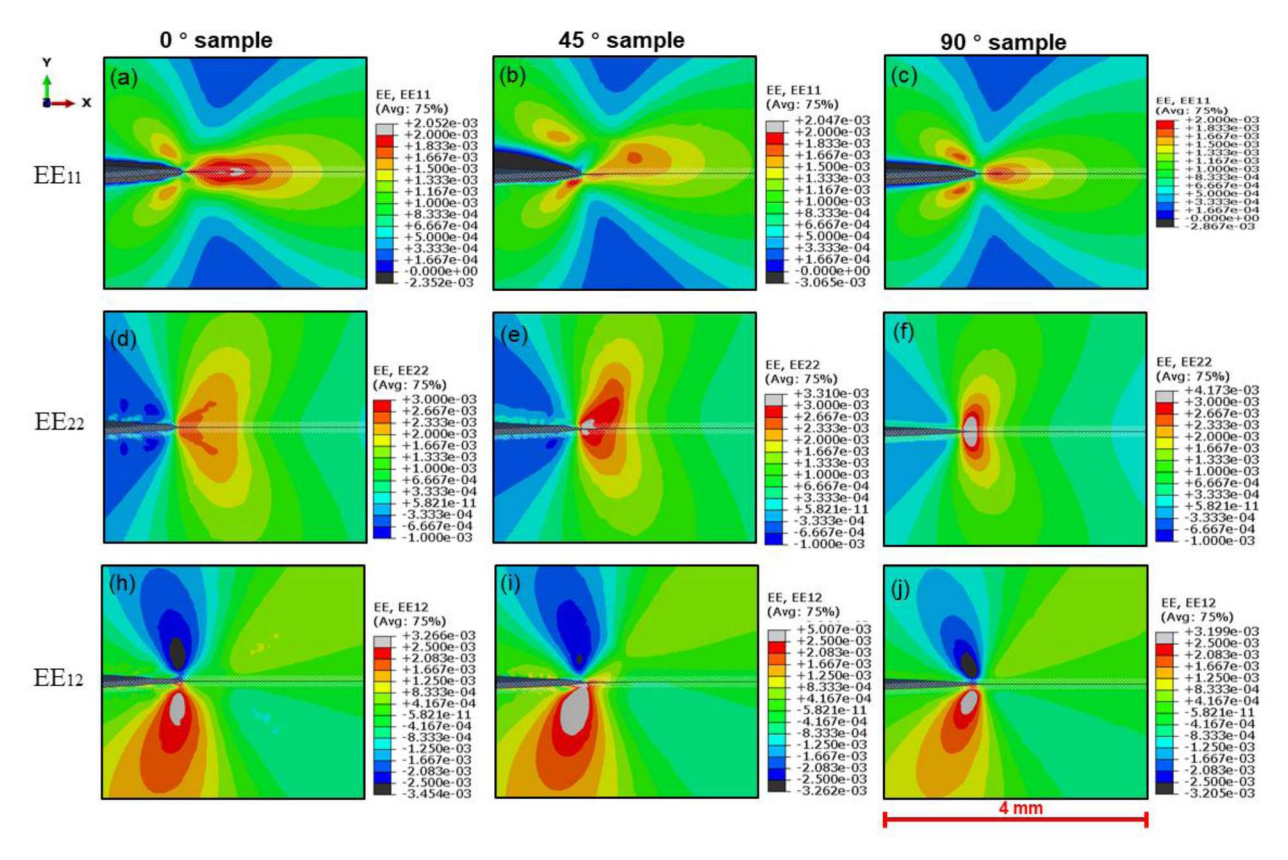


Fig. 14. (a–c) Contours of elastic strains along the crack growth direction, EE_{11} ; (d–f) contours of elastic strains along the crack opening direction, EE_{22} ; and (h–j) contours of shear strain, EE_{12} , at K_{max} under plane-stress condition for the 0° sample, 45° sample, and 90° sample from FE simulation. The deformation field is magnified by a factor of 10.

The interface parameters are $\sigma_{max}=820$ MPa, $\delta_n=1$ μm , $\delta_a/\delta_n=0.4$, and $\delta_f/\delta_n=10$, since a large δ_f/δ_n will prevent a rapid softening of K⁺ to slow down the crack growth rate, and a small δ_a/δ_n will ensure that K⁺ approaches K⁻ rapidly during unloading. As illustrated by Tvergaard and Hutchinson (1992), the choice of σ_{max}/σ_y will significantly affect the propagation of crack in the sense that the crack under monotonic loading will not propagate with a large σ_{max} and will grow too fast with a small σ_{max} without forming a fully developed plastic zone, and $\sigma_{max}/\sigma_y\approx 3$ is usually suggested. Zheng et al. (2011) found the choice of cohesive parameters shall not affect the plastic zone size and strain history under a cyclic loading but affect the crack growth rate when the crack bridging zone size is much smaller than the plastic zone. For simplicity, a plastic anisotropic hardening model without any cyclic hardening/softening is considered in this work. From the perspective of illustrating the effect of the plastic anisotropy on the lattice strain fields, local coordinate systems have been defined by rotating 0°, 45°, and 90° about the 3-axis for defining the material properties, which are used to achieve the three same cases in our S-XRD mapping.

The contours of elastic strain, EE_{22} , for the 90° sample from our simulation under plane-strain and plane-stress conditions are shown in Fig. 13. By comparing the amplitude and distribution of the strain, we can see the plane-stress results agree well with the experimental data, while the plane-strain results underestimated the crack tip strains. This indicates that the sample was sufficiently thin to achieve a near-true plane-stress condition at K_{max} .

Contours of the elastic strain components (EE₁₁, EE₂₂, and EE₁₂) and stress components (S_{11} , and S_{22}) near the crack tip at the K_{max} with a crack length of 9 mm under plane-stress condition for the above three cases are plotted in Fig. 14 and Fig. 15, respectively. The crack tip location is determined when the crack opening displacement reaches δ_n . Obviously, the shapes of these contours are consistent with our S-XRD experimental results: a squid-shaped tensile elastic strain field, EE₁₁, is developed along the crack growth path; a dumbbell-shaped tensile elastic strain field, EE₂₂, is observed ahead of the fatigue crack tip with a compressive strain field, EE₂₂, behind the crack tip; and a butterfly-shaped elastic strain field, EE₁₂, is noticed around the crack tip. Similar to our experimental results, the 90° sample exhibits the largest S_{22} / EE₂₂ fields, and the asymmetric character of the lattice strain/stress fields in the 45° sample is also captured by the cohesive interface model by applying Hill's anisotropic plasticity model. The peak stress/strain amplitude agrees well with our S-XRD experimental results. Meanwhile, the crack extension, Δa , versus the number of cycles, N, is plotted in Fig. 16 for the above three cases from our simulation. The slopes of these curves indicate the fatigue crack growth rate (da/dN). It is clear to see that when the steady fatigue crack is achieved, the 0° sample shows the smallest slope, and the 90 sample exhibits the greatest crack growth rate, which is consistent with the response in our fatigue crack growth test. However, the tensile strain (stress) field, EE₁₁ (S₁₁), in the plastic wake region is not captured by the simulation. This discrepancy can be related to the limit of our

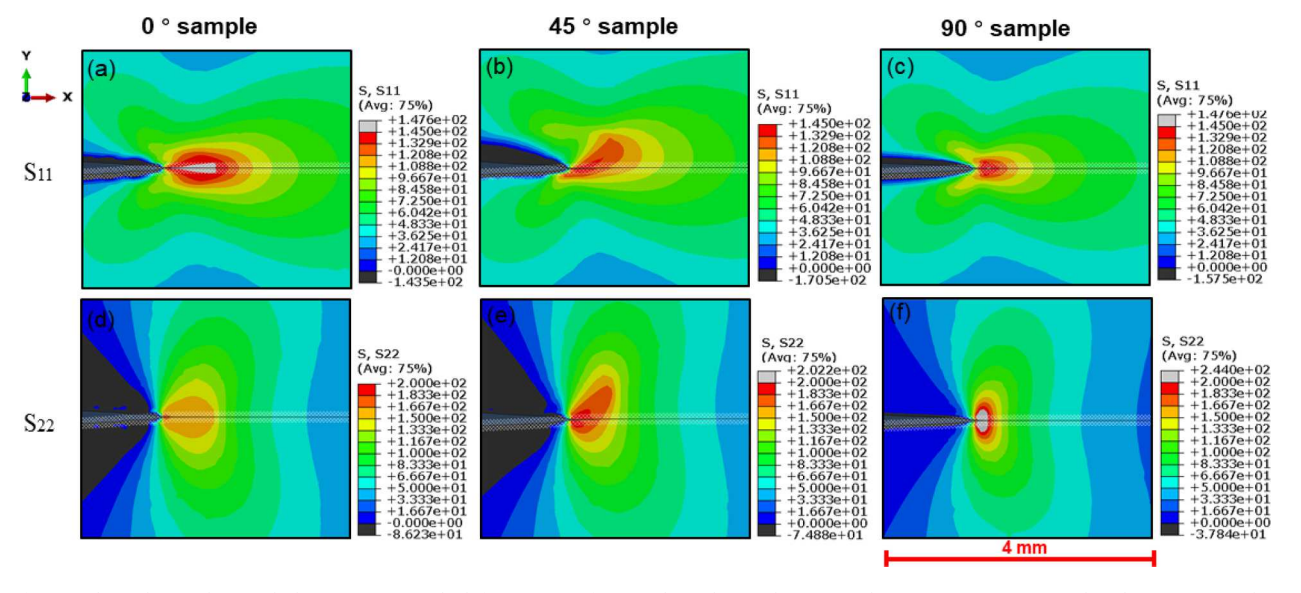


Fig. 15. (a–c) Contours of stress along the crack growth direction, S_{11} ; and (d–f) contours of stress along the crack opening direction, S_{22} , at K_{max} under plane-stress condition for the 0° sample, and 90° sample from FE simulation. The deformation field is magnified by a factor of 10.

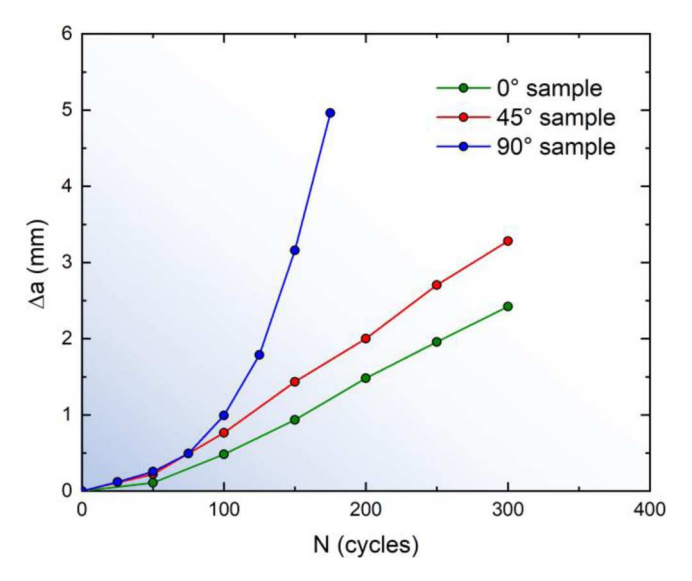


Fig. 16. The crystal plasticity finite element setup for a notched CT specimen to mimic the blunted fatigue crack tip. The geometric sizes are taken from Fig. 3.

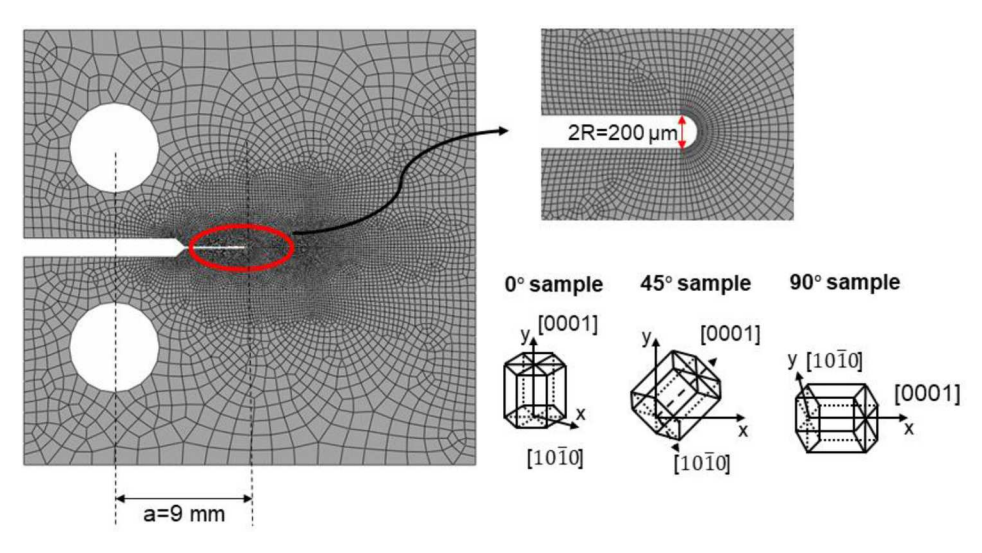


Fig. 17. Crack extensions, Δa , plotted against the number of cycles, N, for the three cases from FE simulation.

model, where the deformation twinning and texture evolution induced by the twinning process are not considered.

It should be noted again that the employed cohesive interface model is of a phenomenological nature with the sole purpose being to generate a steady fatigue crack. To achieve this objective, we need to ensure that the crack bridging zone size and the crack increment per cycle are significantly smaller than the plastic zone size. To this end, we can easily adjust the parameters used in the plasticity model to attain a good agreement between the simulated and measured "clean" plastic zones in Figs. 7 and 14 even for this heavily textured and plastically anisotropic material, but the "messy" process zone at the crack tip (within half of R_p) shows some noticeable discrepancies. This difference can actually be used as inputs for an inverse problem to extract a mechanism-based cohesive zone law, but this will be left for future work.

3.4.2. Crystal plasticity finite element simulations of twin distributions

In ductile materials, the propagation of fatigue crack during the cyclic loading involves the progressively plastic blunting of the crack tip on loading and resharpening on unloading (Ritchie, 1999). The crack tip can be simplified as a notch instead of a sharp crack based on the plastic zone size. A 2-D finite element analysis on a standard CT sample with a long crack (crack length = 9 mm, crack root radius = $100 \, \mu m$) is considered under a monotonic loading to P_{max} . Fatigue loading conditions are not computed here as detwinning is not included in the above crystal plasticity finite element constitutive model. As will be shown shortly, this limitation does not prevent us from understanding the texture dependence of twin distributions.

Table 3

The initial and final critical resolve shear stresses used in the HCP crystal plasticity finite element model, as estimated from Wu et al. (2008).

	Basal <a> slip	Prismatic $<$ a $>$ slip	Pyramidal <a> slip	Pyramidal $< a+c > $ slip	Extension Twinning	Compression Twinning
τ_0	8	113 MPa	n/a	n/a	58 MPa	n/a
$ au_s$	8	113 MPa	n/a	n/a	58 MPa	n/a

The finite element mesh for simulation is shown in Fig. 17, with the same geometry of the CT sample in Fig. 3(a). As previously mentioned, the difference of the "twin band" is primarily dominated by the twinning/detwinning behavior in A-grains in these samples, the grain orientations in the simulation are consistent with the A-grains in these samples. Based on the initial strong $\{0001\}<10\overline{1}0>$ rolling texture, for simplicity, the CT specimen is assumed to be a single crystal, where the crack growth direction is along $[10\overline{1}0]$ -direction, the crack opening direction is along [0001] in the 0° sample; compared to the 0° sample, the crystal lattice rotates 45° clockwise on the $[10\overline{1}0]$ -[0001] plane in the 45° sample; the crack growth direction is along the [0001], the crack opening direction is along $[10\overline{1}0]$ in the 90° sample. For all three samples, the normal to the flat surface of the notch is aligned $[\overline{1}2\overline{1}0]$. In our calculations, the elastic constants of the ZK60 Mg alloy is given as $C_{11} = 59.3$ GPa; $C_{12} = 25.7$ GPa; $C_{13} = 21.4$ GPa; $C_{33} = 61.5$ GPa; $C_{55} = 16.4$ GPa (Hearmon, 1984). The hardening parameters used in the HCP crystal plasticity model are estimated from Ref. Wu et al. (2008), as listed in Table 3, where only basal slip, prismatic slip, and extension twinning are considered. And the parameters for the twinned fraction are given by $s_{th} = 170$ MPa; s = 220 MPa; $\dot{e}_0 = 0.001s^{-1}$; m = 0.07.

The contours of the extension twinning volume fraction of the three samples are shown in Fig. 18 at a load level of P=650 N. The distributions of the extension twinning are distinctively different in the above three cases. The extension twinning predominantly occurs in a small region ahead of the notch tip for the 0° sample, which has a symmetric shape on the crack growth plane. The calculation results by our explicit finite element method are qualitatively the same as the 3D finite element simulations by Kaushik et al. (2014) that the extension twin distributions are near the notch root. However, unlike the 0° sample, the contour of extension twinning is asymmetric on the crack growth plane in the 45° sample. The extension twinning activity occurs prevailing in the lower left quarter of the notch, which is associated with the strong plastic anisotropic response in this ZK60 Mg alloy. Whereas in the 90° sample, in contrast to the 0° and 45° samples, the activation of extension twins spread in the vicinity of fatigue crack surfaces behind the notch tip instead of the notch root.

Clearly, the distribution of extension twinning is strongly crystallographic orientation-dependent, which shows very good agreement with the S-XRD results in Fig. 12. We can also notice that the region near the notch root experiences high levels of twin volume f_T in all three samples. As noted above, extension twinning occurs around the crack root in all three samples with far-field tensile stress. Based on the simulation results, it is reasonable to anticipate that the formation of a narrow "twin band" along the crack growth path during the progressive extension of the fatigue crack is attributed to the accumulation of residual extension twins formed around the crack root, although the extension twinning is more prevailing behind the crack tip in the 90° sample.

4. Discussion

In our direct strain measurement by *in situ* S-XRD measurement, the stress state at the crack tip is not uniaxial, but a non-equal biaxial tension at K_{max} , as displayed in Fig. 9. This biaxial tension at the crack tip can facilitate the occurrence of extension twinning in these samples, even though the stress level, S_{22} , in the 90° sample is even lower than the yield strength along ED. This is consistent with previous reports (Cheng et al., 2020; Xia et al., 2020). Cheng et al. (2020) reported that biaxial tension can increase the difference in the Schmid factor for the six twin variants and make Schmid law more efficient, and twin variant selection and volume fraction are highly dependent on the directional strength ratio. Xia et al. (2020) suggested that the activity of extension twins was increased under the biaxial compressive stress state, compared with the uniaxial stress state, since the equivalent yield strength under a biaxial compressive stress state was lower than that under a uniaxial stress state. The higher I{0002} in the 90° sample behind the crack tip can be attributed to the non-equal biaxial compression-tension stress/strain state behind the crack tip, where tensile stress S_{11} along the c-axis and compressive stress S_{22} perpendicular to the c-axis of the A-grain favor the activation of extension twinning in these A-grains. Our FEM result for the twin distribution also predicts that the extension twinning predominantly occurs behind the crack tip in the 90° sample, as shown in Fig. 18. The synergy analysis of the stress and intensity evolution along the "twin band" indicates the activation of extension twinning depends on the collective of local stress state and texture (Han et al., 2014; Hou et al., 2018).

In terms of the relatively low threshold value and high crack growth rate under the same ΔK value in the 90° sample and 45° sample, three affected factors are proposed here. Firstly, as shown in Figs. 7 and 9, with the same K value, the 90° sample has the largest stress/strain fields ahead of the crack tip at K_{max} , followed by the 45° sample. The difference between the magnitude of stress/strain at the crack tip due to the sample orientations shall act as an important factor that affects the fatigue crack growth rate, as high stress/strain level at the crack tip facilitates the damage initiation and crack propagation, resulting in the high fatigue crack growth rate. Secondly, the reverse plastic zone with greater zone size and magnitude is developed in the 0° sample at K_{min} , as displayed in Fig. 8, compared with the other two samples. Analogous to the overload effect on the fatigue resistance (Huang et al., 2012; Lam et al., 2020),

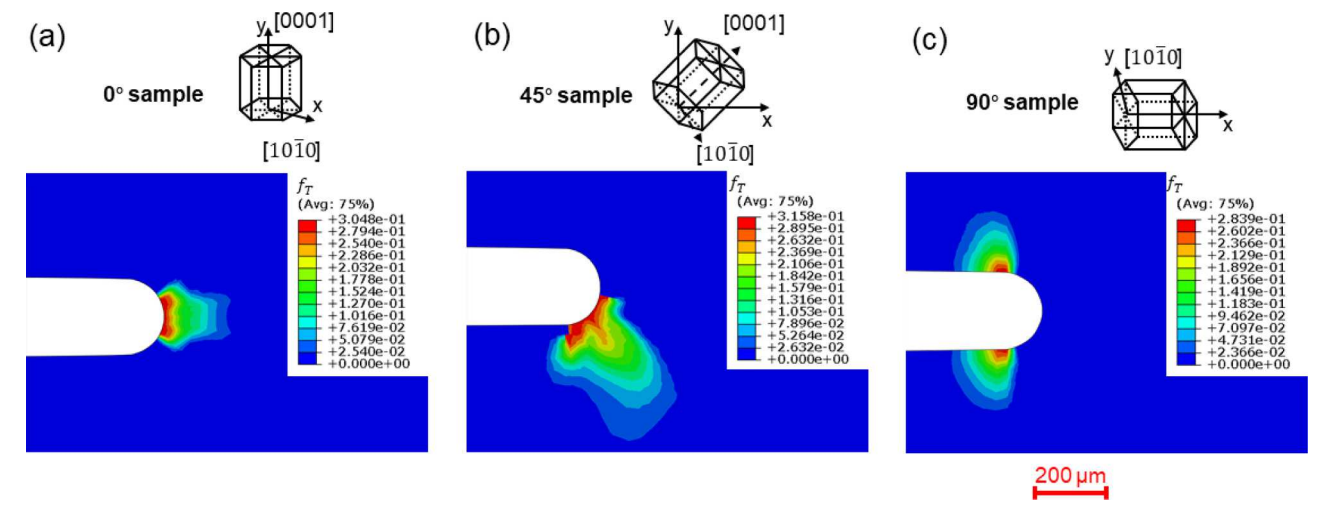


Fig. 18. Contours of the extension twin fraction near the crack root for (a) 0° sample, (b) 45° sample, and (c) 90° sample from FE simulation.

the relatively large compressive stress field at the crack tip can significantly decrease the effective crack-opening load and cause the crack-growth retardation in the 0° sample. Thirdly, the higher extent of accumulated deformation twins would facilitate the initiation and the early growth of fatigue crack in the 90° sample and 45° sample (Briffod et al., 2019). The fatigue deformation of Mg alloys is strongly affected by the interaction between deformation twin and dislocation slip (Basha et al., 2018). The high deformation incompatibility between matrix and twin will impede dislocation movement and result in high local stress, which promotes the creation of cracks (Yang et al., 2008a, 2011b; Xu and Han, 2013). More twins that are observed in the 90° sample and 45° sample during the fatigue crack growth will result in more cyclic deformation irreversibility and cumulative fatigue damage, which lead to a relatively low threshold value for crack propagation and worse fatigue performance, especially in the 90° sample (Prasad et al., 2015). In this regard, deformation twinning appears to be detrimental to fatigue property. Our experimental results here can be useful for further simulation, such as the finite element method that considers the twin/detwin process to determine the effect of sample orientation on the twin evolution, stress intensity factors, crack-propagation path, and even the fatigue lifetime.

5. Conclusions

The deformation fields near a crack tip in a ZK60 Mg alloy with different orientations are measured using *in situ* S-XRD, coupled with the cohesive interface and crystal-plasticity finite element simulations. Three CT samples with crystallographic orientations referred to as 0° , 45° , and 90° samples are chosen for this study. Three key conclusions can be derived from these experimental and modeling studies. First, the shapes of lattice strain fields and stress fields exhibit strong dependence on the plastic anisotropy in the ZK60 alloy. This is primarily due to the plastic anisotropy which in turn results from the texture. Using a macroscopic anisotropic plasticity model (i.e., Hill model) is sufficient to predict these experimental findings. Second, extension twinning is observed in the vicinity of the fatigue crack surface and form a "twin band" along the crack growth path in these three samples. The activation of extension twinning is both texture and local stress-state dependent. To our surprise, more grains are involved in the twinning process in the 90° sample with the basal plane aligning the far-field tensile loading direction, and only a few twins are observed in the 0° sample with the c-axis along the loading direction. Nevertheless, twins have little contribution to the anisotropic lattice-strain fields essentially because of narrow twin bands. Using a simplified CPFEM model for Mg alloy to simulate the distribution of extension twinning near a crack root, the observation of the "twin band" along the crack growth path can be partly explained. Third, compared with the 0° sample, the collective effect of relatively high stress/strain fields ahead of a crack tip at K_{max} , low reverse compressive stress field distribution at a crack tip at K_{min} , and a large extent of deformation twins involved in the crack extension in the 90° and 45° sample contributes to more cyclic deformation irreversibility and cumulative fatigue damage, leading to the weak fatigu

Declaration of Competing Interest

The authors declare no competing interests.

Acknowledgments

This work is supported by the US National Science Foundation (DMR 1809640 to the University of Tennessee & DMR 1809696 to the University of Illinois). DX also acknowledges a graduate fellowship from Center for Materials Processing at the University of Tennessee. This research used resources of the Advanced Photon Source, a U.S. Department of Energy (DOE) Office of Science User Facility operated for the DOE Office of Science by Argonne National Laboratory under Contract No. DE-AC02-06CH11357.

Appendix

A.1. Twin observation near a crack tip

In order to further confirm the distribution of twins near a fatigue crack tip, optical microscopic (OM) micrographs are captured around the crack tip for the 0° sample, 45° sample, and 90° sample. From Fig. S1, we can see that a large volume of twins spread in the 90° sample, a relatively small number of twins in the 45° sample, only a few twins in the 0° sample, which are consistent with the intensity analysis. We can also note that deformation twins are mainly developed in the large matrix colony where the Mg matrix exhibits close crystal orientation and provides the beneficial crystallographic spaces for twin growth, and the twin growth is restricted by the grain boundary or colony boundary, as seen in Fig. S1. Twins have also been found near the crack surfaces in the plastic wake, so that an averaged measurement such as the S-XRD will rather see the "twin band" in Fig. 12. In other words, images in Fig. S1 compare favorably to the CPFEM simulation results in Fig. 18, while the collective behavior of twins in the plastic wake correspond to the findings in Fig. 12.

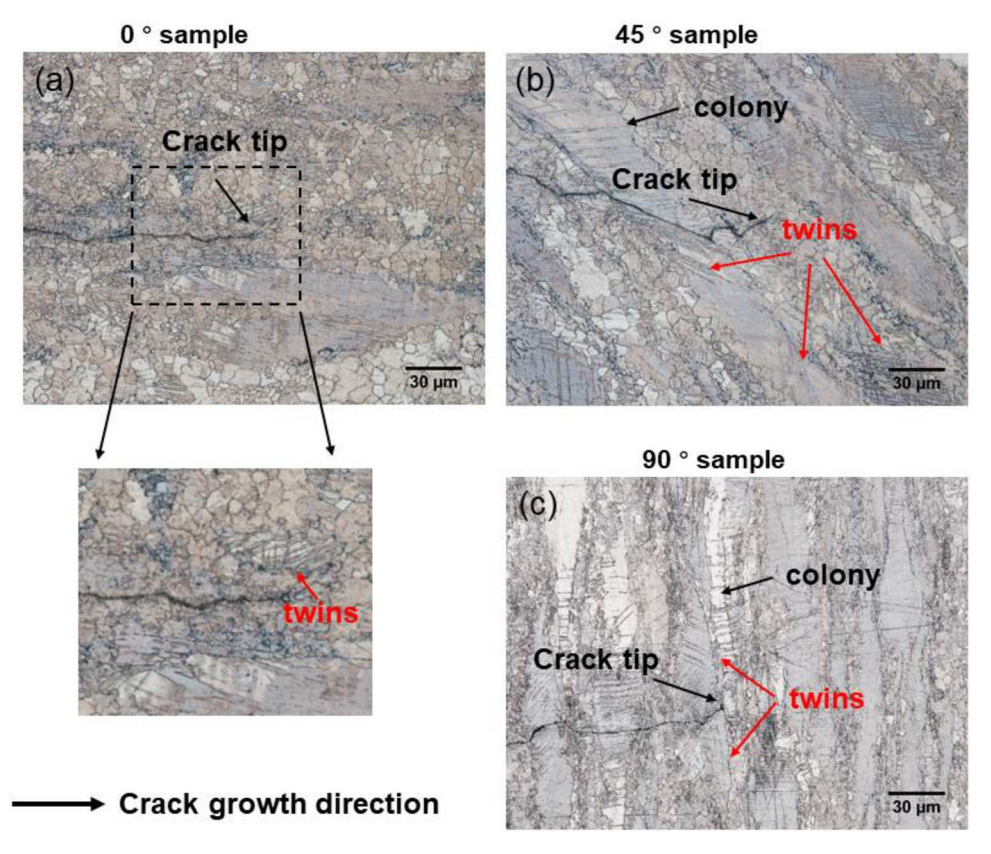


Fig. S1. Optical micrographs around the crack tip for (a) the 0° sample, (b) 45° sample, and (c) 90° sample after S-XRD mapping. Red arrows point out the twins and colony, and black arrows point out the crack.

A.2. Crystal plasticity finite element model

In the crystal plasticity finite element method, the volume fraction of twins for the i-th twin system is a field parameter, denoted as f^i , which satisfies $f^i \ge 0$, with $\xi = \sum f^i \le 1$ (i = 1, 2,..., N_t , where N_t is the total number of twin systems).

The constitutive relationship between stress and strain in a metallic single crystal is taken as a linear relation as following:

$$T^e = C[E^e] \tag{S-1}$$

where C is a fourth-order anisotropic elasticity tensor, E^e and T^e are the Green elastic strain measure and the symmetric second Piola–Kirchoff stress tensor related to the relaxed configuration, given in terms of the elastic deformation gradient F^e ,

$$E^{e} = (1/2)\{F^{eT}F^{e} - I\}$$
 (S-2)

$$T^{e} = (detF^{e})F^{e-1}TF^{e-T}$$
(S-3)

The Schmid tensors for the i-th slip/twin system, S_0^i , are described in terms of a unit normal n_0^i to the slip/twin plane and a unit vector m_0^i denoting the slip/twin direction,

$$S_0^i = m_0^i \otimes n_0^i$$
 (S-4)

The conditions for slip and twinning are restricted by the resolved shear stress, T^i , and slip/twin system deformation resistances, s^i , on the i-th slip/twin system:

$$T^{i} = (C^{e}T^{e}) \cdot S_{0}^{i} \tag{S-5}$$

$$\phi^i = |\tau^i| - s^i \le 0 \tag{S-6}$$

The flow rule described by the evolution of the plastic deformation gradient due to crystallographic slip and twinning is taken as:

$$\dot{\mathbf{F}}^p = L^p F^p$$
 (S-7)

In this equation, L^p is the sum of the shearing rates on all the slip and twin systems, given by:

$$L^{p} = \sum \dot{\gamma} sign(\tau^{i})S_{0}^{i} \tag{S-8}$$

And the shearing rates are restricted as follows:

$$\dot{\gamma}^i \ge 0$$
, and $\dot{\gamma}^i \phi^i = 0$, if $\phi^i = 0$. (S-9)

For the twinning plasticity, a composite sum is assumed in which the twinned fraction deforms by a Mises plasticity, and the untwinned fraction assumes Eq. (S-8). Thus, slip bands and twin lamella of the crystal are not explicitly considered in this type of model. The flow rule is now written as

$$L^{p} = (1 - \xi) \sum_{i} \dot{\gamma} sign(\tau^{i}) S_{0}^{i} + \xi M$$
 (S-10)

$$\mathbf{M} = \dot{\varepsilon}_0 \left\{ \frac{\overline{\sigma} - s_{th}}{s} \right\}^{\frac{1}{m}} \left(\frac{3\mathbf{T}^{es}}{2\overline{\sigma}} \right) \tag{S-11}$$

$$\overline{\sigma} = \sqrt{\frac{3}{2}T^e, T^e},$$
 (S-12)

where s is a strength measure, s_{th} is a threshold value, and T^e , is the deviatoric part of T^e . Note that the "isotropic term" is activated only if the equivalent tensile stress $\overline{\sigma}$ in a grain that exceeds the threshold, s_{th} , which is used to bound the stress levels.

References

ABAQUS Documentation, 2017. Dassault Systèmes. Providence, RI, USA.

Agnew, S.R., Mulay, R.P., Polesak III, F.J., Calhoun, C.A., Bhattacharyya, J.J., Clausen, B., 2013. *In situ* neutron diffraction and polycrystal plasticity modeling of a Mg-Y-Nd-Zr alloy: effects of precipitation on individual deformation mechanisms. Acta Mater. 61, 3769–3780.

ASTM E 647-99, 2022. Standard test Method for Measurement of Fatigue Crack Growth Rates. American Society for Testing and Materials, West Conshohocken, PA. ASTM E399-90, 2021. Standard Test Method for Plane-Strain Fracture Toughness of Metallic Materials. American Society for Testing and Materials, West Conshohocken, PA.

Bachmann, F., Hielscher, R., Schaeben, H., 2010. Texture analysis with MTEX-free and open source software toolbox. Solid State Phenom. 160, 63-68.

Barabash, R.I., Gao, Y.F., Sun, Y., Lee, S., Choo, H., Liaw, P.K., Brown, D.W., Ice, G.E., 2008. Neutron and x-ray diffraction studies and cohesive interface model of the fatigue crack deformation behavior. Philos. Mag. Lett. 88, 553–565.

Basha, D.A., Somekawa, H., Singh, A., 2018. Crack propagation along grain boundaries and twins in Mg and Mg–0.3 at.% Y alloy during *in-situ* straining in transmission electron microscope. Scr. Mater. 142, 50–54.

Briffod, F., Shiraiwa, T., Enoki, M., 2019. Numerical investigation of the influence of twinning/detwinning on fatigue crack initiation in AZ31 magnesium alloy. Mater. Sci. Eng. A 753, 79–90.

Brown, D.W., Agnew, S.R., Bourke, M.A.M., Holden, T.M., Vogel, S.C., Tomé, C.N., 2005. Internal strain and texture evolution during deformation twinning in magnesium. Mater. Sci. Eng. A 399, 1–12.

Catoor, D., Gao, Y.F., Geng, J., Prasad, M.J.N.V., Herbert, E.G., Kumar, K.S., Pharr, G.M., George, E.P., 2013. Incipient plasticity and deformation mechanisms in single-crystal Mg during spherical nanoindentation. Acta Mater. 61, 2953–2965.

Cheng, Y., Fu, Y., Xin, Y., Chen, G., Wu, P., Huang, X., Liu, Q., 2020. {1012} twinning behavior under biaxial tension of Mg–3Al–1Zn plate. Int. J. Plast. 132, 102754. Chew, H.B., Hong, S.S., Kim, K.S., 2009. Cohesive-zone laws for void growth – II. Numerical field projection of elasto-plastic fracture processes with vapor pressure. J. Mech. Phys. Solids 57, 1374–1390.

Gao, Y.F., Bower, A.F., 2004. A simple technique for avoiding convergence problems in finite element simulations of crack nucleation and growth on cohesive interfaces. Model. Simul. Mater. Sci. Eng. 12, 453–463.

Gao, Y.F., 2016. Deformation fields near a steady fatigue crack with anisotropic plasticity. Extreme Mech. Lett. 6, 45-51.

Gharghouri, M.A., Weatherly, G.C., Embury, J.D., Root, J., 1999. Study of the mechanical properties of Mg-7.7 at.% Al by *in-situ* neutron diffraction. Philos. Mag. A 79, 1671–1695.

Han, Z., Luo, H., Sun, C., Li, J., Papaelias, M., Davis, C., 2014. Acoustic emission study of fatigue crack propagation in extruded AZ31 magnesium alloy. Mater. Sci. Eng. A 597, 270–278.

R.F.S. Hearmon, 1946, The Elastic Constants of Anisotropic Materials, Rev. Mod. Phys. 18, 409.

Hill, R., 1948. A variational principle of maximum plastic work in classical plasticity. Q. J. Appl. Math. 1, 18–28.

Hong, S.S., Chew, H.B., Kim, K.S., 2009. Cohesive-zone laws for void growth – I. Experimental field projection of crack-tip crazing in glassy polymers. J. Mech. Phys. Solids 57, 1357–1373.

Hono, K., Mendis, C.L., Sasaki, T.T., Oh-ishi, K., 2010. Towards the development of heat-treatable high-strength wrought Mg alloys. Scr. Mater. 63, 710–715. Hou, M., Zhang, H., Fan, J., Zhang, Q., Wang, L., Dong, H., Xu, B., 2018. Microstructure evolution and deformation behaviors of AZ31 Mg alloy with different grain orientation during uniaxial compression. J. Alloy. Compd. 741, 514–526.

Huang, E.W., Li, K.W., Lee, S.Y., Woo, W.C., Ding, Y.S., Tsay, L.W., Chen, C.H., 2012. Residual strain distribution around a fatigue-crack tip determined by neutron diffraction. Mater. Sci. Forum 706-709, 1685–1689.

Kaushik, V., Narasimhan, R., Mishra, R.K., 2014a. Experimental study of fracture behavior of magnesium single crystals. Mater. Sci. Eng. A 590, 174-185.

Kaushik, V., Narasimhan, R., Mishra, R.K., 2014b. Finite element simulations of notch tip fields in magnesium single crystals. Int. J. Fract. 189, 195-216.

Kerr, M., Daymond, M.R., Holt, R.A., Almer, J.D., 2010. Mapping of crack tip strains and twinned zone in a hexagonal close packed zirconium alloy. Acta Mater. 58, 1578–1588

Kim, W.J., Hong, S.I., Kim, Y.S., Min, S.H., Jeong, H.T., Lee, J.D., 2003. Texture development and its effect on mechanical properties of an AZ61 Mg alloy fabricated by equal channel angular pressing. Acta Mater. 51, 3293–3307.

King, A., Ludwig, W., Herbig, M., Buffière, J.Y., Khan, A.A., Stevens, N., Marrow, T.J., 2011. Three-dimensional in situ observations of short-fatigue crack growth in magnesium. Acta Mater. 59, 6761–6771.

Kleiner, S., Uggowitzer, P.J., 2004. Mechanical anisotropy of extruded Mg-6% Al-1% Zn alloy. Mater. Sci. Eng. A 379, 258-263.

- Koike, J., Sato, Y., Ando, D., 2008. Origin of the anomalous {10\\bar12} twinning during tensile deformation of Mg alloy sheet. Mater. Trans. 49, 2792–2800.
- Lam, T.N., Lee, S.Y., Tsou, N.T., Chou, H.S., Lai, B.H., Chang, Y.J., Feng, R., Kawasaki, T., Harjo, S., Liaw, P.K., Yeh, A.C., Li, M.J., Cai, R.F., Lo, S.C., Huang, E.W., 2020. Enhancement of fatigue resistance by overload-induced deformation twinning in a CoCrFeMnNi high-entropy alloy. Acta Mater. 201, 412–424.
- Lee, S.Y., Sun, Y., An, K., Choo, H., Hubbard, C.R., Liaw, P.K., 2010a. Evolution of residual-strain distribution through an overload-induced retardation period during fatigue-crack growth. J. Appl. Phys. 107, 023517.
- Lee, S.Y., Choo, H., Liaw, P.K., An, K., Hubbard, C.R., 2011b. A study on fatigue crack growth behavior subjected to a single tensile overload: part II. Transfer of stress concentration and its role in overload-induced transient crack growth. Acta Mater. 59, 495–502.
- Liu, S.F., Wu, Y., Wang, H.T., He, J.Y., Liu, J.B., Chen, C.X., Liu, X.J., Wang, H., Lu, Z.P., 2018. Stacking fault energy of face-centered-cubic high entropy alloys. Intermetallics 93, 269–273.
- Lutterotti, L., Matthies, S., Wenk, H.R., Schultz, A.S., Richardson Jr, J.W., 1997. Combined texture and structure analysis of deformed limestone from time-of-flight neutron diffraction spectra. J. Appl. Phys. 81, 594–600.
- Nguyen, O., Repetto, E.A., Ortiz, M., Radovitzky, R.A., 2001. A cohesive model of fatigue crack growth. Int. J. Fatigue 110, 351-369.
- Pippan, R., Hohenwarter, A., 2017. Fatigue crack closure: a review of the physical phenomena. Fatigue Fract. Eng. Mater. Struct. 40, 471-495.
- Prasad, N.S., Kumar, N.N., Narasimhan, R., Suwas, S., 2015. Fracture beahvior of magneisum alloys role of tensile twinning. Acta Mater. 94, 281-293.
- Qiao, H., Barnett, M.R., Wu, P.D., 2016. Modeling of twin formation, propagation and growth in a Mg single crystal based on crystal plasticity finite element method. Int. J. Plast. 86, 70–92.
- Ritchie, R.O., 1999. Mechanisms of fatigue-crack propagation in ductile and brittle solids. Int. J. Fract. 100, 55–83.
- Sofinowski, K., Panzner, T., Kubenova, M., Čapek, J., Van Petegem, S., Van Swygenhoven, H., 2019. *In situ* tension-tension strain path changes of cold-rolled Mg AZ31B. Acta Mater. 164, 135–152.
- Staroselsky, A., Anand, L., 2003. A constitutive model for hcp materials deforming by slip and twinning. Int. J. Plast. 19, 1843-1864.
- Steuwer, A., Rahman, M., Shterenlikht, A., Fitzpatrick, M.E., Edwards, L., Withers, P.J., 2010. The evolution of crack-tip stresses during a fatigue overload event. Acta Mater. 58, 4039–4052.
- Toby, B.H., Von Dreele, R.B., 2013. GSAS-II: the genesis of a modern open-source all purpose crystallography software package. J. Appl. Crystallogr. 46, 544–549. Tvergaard, V., Hutchinson, J.W., 1992. The relation between crack growth resistance and fracture process parameters in elastic-plastic solids. J. Mech. Phys. Solids 40, 1377–1397.
- Wang, Z., Hao, X., Qiu, J., Jin, T., Shu, X., Li, X., 2020. Anisotropic yield criterion of rolled AZ31 magnesium alloy via nanoindentation. Appl. Sci. 10, 8997.
- Withers, P.J., 2015. Fracture mechanics by three-dimensional crack-tip synchrotron X-ray microscopy. Philos. Trans. R. Soc. A 373, 20130157.
- Wu, L., Agnew, S.R., Brown, D.W., Stoica, G.M., Clausen, B., Jain, A., Fielden, D.E., Liaw, P.K., 2008. Internal stress relaxation and load redistribution during the twinning-detwinning-dominated cyclic deformation of a wrought magnesium alloy, ZK60A. Acta Mater. 56, 3699–3707.
- Wu, L., Jain, A., Brown, D.W., Stoica, G.M., Agnew, S.R., Clausen, B., Fielden, D.E., Liaw, P.K., 2008c. Twinning–detwinning behavior during the strain-controlled low-cycle fatigue testing of a wrought magnesium alloy, ZK60A. Acta Mater. 56, 688–695.
- Wu, W., Lee, S.Y., Paradowska, A.M., Gao, Y., Liaw, P.K., 2012a. Twinning-detwinning behavior during fatigue-crack propagation in a wrought magnesium alloy AZ31B. Mater. Sci. Eng. A 556, 278–286.
- Wu, W., Liaw, P.K., An, K., 2015. Unraveling cyclic deformation mechanisms of a rolled magnesium alloy using *in situ* neutron diffraction. Acta Mater. 85, 343–353. Wu, Y., Stoica, A.D., Ren, Y., Ma, D., Gao, Y.F., Bei, H., 2015. Direct synchrotron x-ray measurements of local strain fields in elastically and plastically bent metallic glasses. Intermetallics 67, 132–137.
- Wu, W., Gao, Y.F., Li, N., Parish, C.M., Liu, W.J., Liaw, P.K., An, K., 2016. Intragranular twinning, detwinning, and twinning-like lattice reorientation in magnesium alloys. Acta Mater. 121, 15–23.
- Wu, W., Chuang, C.-P., Qiao, D., Ren, Y., An, K., 2016b. Investigation of deformation twinning under complex stress states in a rolled magnesium alloy. J. Alloy. Compd. 683, 619–633.
- Xia, D., Zhang, J., Chen, X., Huang, G., Jiang, B., Tang, A., Gavras, S., Huang, Y., Hort, N., Pan, F., 2020. Effect of biaxial compressive stress state on the microstructure evolution and deformation compatibility of rolled sheet Mg alloy AZ31 at room temperature. Mater. Sci. Eng. A 789, 139599.
- Xie, D., Lyu, Z., Li, Y., Liaw, P.K., Chew, H.B., Ren, Y., Chen, Y., An, K., Gao, Y., 2021. *İn situ* monitoring of dislocation, twinning, and detwinning modes in an extruded magnesium alloy under cyclic loading conditions. Mater. Sci. Eng. A 806.
- Xu, D.K., Han, E.H., 2013. Relationship between fatigue crack initiation and activated {101 2} twins in as-extruded pure magnesium. Scr. Mater. 69, 702–705. Yang, F., Yin, S.M., Li, S.X., Zhang, Z.F., 2008a. Crack initiation mechanism of extruded AZ31 magnesium alloy in the very high cycle fatigue regime. Mater. Sci. Eng. A 491, 131–136.
- Yang, F., Lv, F., Yang, X.M., Li, S.X., Zhang, Z.F., Wang, Q.D., 2011b. Enhanced very high cycle fatigue performance of extruded Mg-12Gd-3Y-0.5 Zr magnesium alloy. Mater. Sci. Eng. A 528, 2231–2238.
- Yin, D.D., Boehlert, C.J., Long, L.J., Huang, G.H., Zhou, H., Zheng, J., Wang, Q.D., 2021. Tension-compression asymmetry and the underlying slip/twinning activity in extruded Mg-Y sheets. Int. J. Plast. 136, 102878.
- Zhai, T., Wilkinson, A.J., Martin, J.W., 2000. A crystallographic mechanism for fatigue crack propagation through grain boundaries. Acta Mater. 48, 4917–4927.
- Zhang, J., Yu, Q., Jiang, Y., Li, Q., 2011a. An experimental study of cyclic deformation of extruded AZ61A magnesium alloy. Int. J. Plast. 27, 768–787.
- Zhang, H., Jérusalem, A., Salvati, E., Papadaki, C., Fong, K.S., Song, X., Korsunsky, A.M., 2019c. Multi-scale mechanisms of twinning-detwinning in magnesium alloy AZ31B simulated by crystal plasticity modeling and validated via *in situ* synchrotron XRD and *in situ* SEM-EBSD. Int. J. Plast. 119, 43–56.
- Zhang, M., Zhang, H., Ma, A., Llorca, J., 2021b. Experimental and numerical analysis of cyclic deformation and fatigue behavior of a Mg-RE alloy. Int. J. Plast. 139. Zheng, L.L., Gao, Y.F., Lee, S.Y., Barabash, R.I., Lee, J.H., Liaw, P.K., 2011. Intergranular strain evolution near fatigue crack tips in polycrystalline metals. J. Mech. Phys. Solids 59, 2307–2322.
- Zhou, N., Zhang, Z., Jin, L., Dong, J., Chen, B., Ding, W., 2014. Ductility improvement by twinning and twin-slip interaction in a Mg-Y alloy. Mater. Des. 56, 966–974 (1980-2015).
- Zou, Y., Zhang, L., Li, Y., Wang, H., Liu, J., Liaw, P.K., Bei, H., Zhang, Z., 2018. Improvement of mechanical behaviors of a superlight Mg-Li base alloy by duplex phases and fine precipitates. J. Alloy. Compd. 735, 2625–2633.